The Astrophysical Journal, 997:283 (18pp), 2026 February 1 https://doi.org/10.3847/1538-4357/ae22cf

Two Epochs of VLBI Observations of Eight KISSR Seyfert and LINER Galaxies: Suggestions of Fast and Filamentary Outflows

Preeti Kharb[1], Anderson Caproni[2], Salmoli Ghosh[1], Daniel A. Schwartz[3], Mousumi Das[4], Smitha Subramanian[4], and Sravani Vaddi[5]
[1] National Centre for Radio Astrophysics (NCRA)—Tata Institute of Fundamental Research (TIFR), S. P. Pune University Campus, Ganeshkhind, Pune 411007, Maharashtra, India; kharb@ncra.tifr.res.in
[2] Núcleo de Astrofísica, Universidade Cidade de São Paulo, R. Galvão Bueno 868, Liberdade, São Paulo, SP, 01506-000, Brazil
[3] Center for Astrophysics | Harvard & Smithsonian, 60 Garden Street, Cambridge, MA 02138, USA
[4] Indian Institute of Astrophysics, 2nd Block, Koramangala, Bangalore 560034, India
[5] Arecibo Observatory: Arecibo, Puerto Rico, USA
Received 2025 May 28; revised 2025 November 18; accepted 2025 November 19; published 2026 January 28

Abstract

We present here the results from a second epoch of phase-referenced VLBA observations of eight Seyfert and LINER galaxies from the KISSR sample. These sources were chosen based on the presence of double peaks or asymmetries in their emission lines as observed in SDSS spectra. Parsec-scale radio emission is detected in seven of the eight sources in the second epoch. Jet-like features appear to persist over a ∼4–9 yr timeline in these "radio-quiet" AGN. A few sources like KISSR1494, however, show significantly different structures after a 9 yr interval. KISSR102, which was previously suggested to be a binary black hole candidate based on the presence of two compact cores, shows the tentative signatures of superluminal jet motion ($1.05 \pm 0.45c$). Tentative superluminal motion in a jet knot has been reported in another source, KISSR872 ($1.65 \pm 0.57c$). We present 1.5 GHz images from the VLA A-array of four sources. These images reveal core-lobe or core-halo structures. The alignment of the VLBI jet direction with the kiloparsec-scale spectral index gradient, as well as the mismatch between the star formation rate derived from the radio and Hα line emission, support the suggestion that the kiloparsec-scale emission is AGN-jet-related. The jets in KISSR sources appear to lose collimation over spatial scales between 200 pc and 1 kpc. Overall, the characteristics of the KISSR jets are reminiscent of similar properties observed in VLBI monitoring studies of "radio-loud" AGN jets even as subtle differences related to the compactness and brightness of jet features remain.

Unified Astronomy Thesaurus concepts: Seyfert galaxies (1447)

1. Introduction

Active galactic nuclei (AGN) are the luminous centers of galaxies that are powered by the release of gravitational potential energy as matter accretes onto supermassive black holes (SMBHs, masses $\sim 10^6$–$10^9\,M_\odot$) through accretion disks (M. J. Rees 1984; B. M. Peterson 1997). Seyfert and low-ionization nuclear emission-line region (LINER) galaxies make up the vast majority of the AGN population (L. C. Ho 2008; T. M. Heckman & P. N. Best 2014). AGN showing only narrow emission lines in their spectra are classified as type 2, while those showing both broad and narrow lines are classified as type 1 (E. Y. Khachikian & D. W. Weedman 1974). It has been postulated that types 1 and 2 differ only by orientation with broad line emission being obscured due to dusty tori (D. E. Osterbrock 1978; R. R. J. Antonucci & J. S. Miller 1985; R. Antonucci 1993). The half opening angle of the obscuring tori may be ∼50° based on the space density of Seyfert types 1 and 2, emission-line bicone images, or X-ray monitoring studies (e.g., L. Woltjer 1990; C. Simpson et al. 1996; H. R. Schmitt et al. 2001; G. Miniutti et al. 2014).

The presence of broad and/or narrow emission lines in the spectra is one of the hallmarks of an AGN. A small fraction of AGN (∼1% in the SDSS[6] survey; J.-M. Wang et al. 2009; X. Liu et al. 2010) show double-peaked emission lines in their spectra. These are referred to as double-peaked AGN (DPAGN). In this paper, we look only at AGN that show double peaks in "narrow" emission lines, whose presence has been suggested to arise either due to the presence of binary SMBHs (predicted in hierarchical galaxy evolution models) with individual associated narrow-line regions or NLRs (H. Zhou et al. 2004; B. F. Gerke et al. 2007), disk-like NLRs (K. L. Smith et al. 2012; R. Nevin et al. 2016; Z. Zhang et al. 2025), NLR kinematics (Y. Shen et al. 2011; H. Fu et al. 2012), gas outflows (T. C. Fischer et al. 2011; J. M. Comerford et al. 2018), jet–NLR interaction (M. Whittle et al. 1988; D. J. Rosario et al. 2010), or a combination of these and other factors (J.-Q. Ge et al. 2012; F. Müller-Sánchez et al. 2015; D. Maschmann et al. 2023).

While Seyferts and LINER galaxies have been categorized as "radio-quiet" (RQ) AGN (K. I. Kellermann et al. 1989; L. C. Ho 2008), very long baseline interferometry (VLBI) observations of Seyfert and LINER galaxies have revealed the presence of weak radio cores and jets in them (H. Falcke et al. 2000; J. S. Ulvestad & L. C. Ho 2001; M. Orienti & M. A. Prieto 2010; A. Doi et al. 2013; R. D. Baldi et al. 2018; P. Kharb et al. 2021). Similarly on arcsecond-scales, 100 parsec-scale and kiloparsec-scale radio structures have been detected as well (S. A. Baum et al. 1993; A. S. Wilson &

[6] Sloan Digital Sky Survey (D. G. York & SDSS Collaboration 2000).

E. J. M. Colbert 1995; E. J. M. Colbert et al. 1996; J. F. Gallimore et al. 2006; P. Kharb et al. 2006; V. V. Rao et al. 2023). While the existence of a clear "radio-loud"/"radio-quiet" AGN divide has been debated (e.g., R. L. White et al. 2000; M. Cirasuolo et al. 2003), and several definitions have been put forth to classify AGN into these RL/RQ AGN categories (e.g., Y. Terashima & A. S. Wilson 2003; K. I. Kellermann et al. 2016; L. Klindt et al. 2019), it is fair to state that RQ AGN have radio jets that typically do not extend beyond the confines of their host galaxies, unlike "radio-loud" AGN.

To understand the nature of the radio outflows in RQ AGN and the origin of double-peaked emission lines, we identified an initial sample of nine type 2 Seyfert and LINER galaxies belonging to the larger KPNO Internal Spectroscopic Red (KISSR) Survey of spiral or disk emission-line galaxies (G. Wegner et al. 2003). These nine sources were selected based on the presence of either double peaks or asymmetries in one or more of the narrow emission lines of [S II], Hα, [N II], or Hβ in SDSS spectra. Sources showing asymmetry only in the [O III] lines were not selected as such asymmetries could be a signature of gas outflows. Additionally, for the feasibility of a VLBI study, a detection in the VLA FIRST[7] survey was a requirement. All sources are unresolved in VLA FIRST images (with the FIRST resolution of $\theta \sim 5''$ translating to spatial scales of $\sim$5–6 kpc in these sources) and had 1.4 GHz radio flux densities ranging from 2.5 to 23.0 mJy. Dual-frequency phase-referenced VLBA observations of these nine DPAGN were carried out from 2013 to 2019 and their results have been presented in P. Kharb et al. (2015, 2017b, 2019, 2020, 2021). We briefly discuss the main results below.

2. Epoch-I VLBI Observations

The first epoch of phase-referenced VLBA observations revealed one-sided parsec-scale jets in 63% or five out of the eight detected sample sources (P. Kharb et al. 2021). One source, viz. KISSR1321, which had the lowest VLA FIRST flux density of 1.6 mJy, was not detected at either frequency with the VLBA. Double radio cores consistent with the presence of binary SMBHs were detected in only one source, viz. KISSR102 (P. Kharb et al. 2020). Explaining jet one-sidedness by Doppler boosting or dimming effects in approaching or receding jets, respectively, implied jet speeds in the range of 0.003–0.75c for assumed jet inclination angles of $\gtrsim$50°; this limit was obtained from their type 2 classification and the expected half opening angle of the dusty torus (P. Kharb et al. 2021). Invoking free–free absorption for the missing counterjet emission presented a difficulty because of the low filling factors of the absorbing gas clouds and the large ($\sim$100 pc-scale) jets observed in several of the sources (see P. Kharb et al. 2019).

Steep radio spectral indices were either observed in both the jets and the "cores" of several sources (e.g., KISSR102, KISSR434, KISSR872) or implied by the nondetection of cores and jets in the higher frequency (i.e., 5 GHz) observations (e.g., KISSR618, KISSR967, KISSR1154, KISSR1219, KISSR1494). In the literature, both flat or inverted radio "core" spectra (e.g., C. G. Mundell et al. 2000; H. Falcke et al. 2000; L. C. Ho 2008; P. Kharb et al. 2017a) and steep "core" spectra (e.g., H. Falcke et al. 2000; A. L. Roy et al. 2000; M. Giroletti & F. Panessa 2009; P. Bontempi et al. 2012; E. Chiaraluce et al. 2019) have been observed in the VLBI images of Seyfert and LINER galaxies.

In this paper, we present the results from second-epoch VLBI observations of the eight (out of the original nine) sources that were detected in the first epoch (P. Kharb et al. 2021). Here, similar to our previous work, we adopt the cosmology with $H_0 = 73\,\mathrm{km\,s^{-1}\,Mpc^{-1}}$, $\Omega_{\mathrm{mat}} = 0.27$, and $\Omega_{\mathrm{vac}} = 0.73$. Spectral index α is defined such that flux density at frequency ν is $S_\nu \propto \nu^{\alpha}$.

3. VLBA Observations

Phase-referenced VLBA observations of eight KISSR galaxies were carried out at 1.5 GHz (Project ID: BK246). As only three of the original nine sources, viz. KISSR102, KISSR434, and KISSR872 were detected at 5 GHz in the first epoch, we reobserved only these three sources at 5 GHz in the second epoch. The VLBA observations were carried out between 2022 September 1 and November 29. Between seven and nine VLBA antennas participated in these experiments. Data were recorded in both bands with a total bandwidth (BW) of 256 MHz (eight intermediate frequencies or IFs with a BW of 32 MHz each) and an aggregate bit rate of 2048 Mbps. Nearby compact sources with accurate small positional uncertainties were used as phase-referencing calibrators (see Table 1). The bright calibrators 4C39.25 and 3C345 were used as fringe-finders. The targets and the phase reference calibrators were observed in a "nodding" mode in a 5 minute cycle (2 minutes on calibrator and 3 minutes on source), for good phase calibration.

In Table 1, we also note the separation between the sources and the recently active Sun. These separations typically ranged between 40° and 70°. The separation was the smallest ($\sim$30°) for KISSR102. The Sun's proximity might have affected the phases in the visibility data of KISSR102 (this source shows the smallest dynamic range in these observations). The small separation of its phase reference calibrator ($1\overset{\circ}{.}78$), however, and the application of ionospheric corrections during the initial calibration using the Astronomical Image Processing Software (`AIPS`; E. W. Greisen 2003) task `TECOR`, were able to mitigate these effects, as was evident from the detection of well correlated phases in KISSR102. The experiment's minimum observing elevation was limited to 8°, in accordance with the constraints applied by the SCHED software while preparing the schedule files.

The data reduction was carried out using the `VLBARUN`[8] procedure in `AIPS`. `VLBARUN` uses the VLBA calibration procedures (`VLBAUTIL`) to calibrate the VLBA data. The calibration steps included a correction of the ionospheric dispersive delays using the task `TECOR` and Earth Orientation Parameters (EOPs) corrections using the task `CLCOR`. After this, amplitude and instrumental delay calibration (using the task `FRING` on a scan of the fringe-finder), followed by a calibration of the bandpass shapes, antenna rates, and phases, was carried out. After parallactic angle corrections, the data were fringe-fit with task `FRING` for a solution interval of 2 minutes. This typically resulted in less than 1% of failed solutions. The fringe-fitting combined the IFs to increase the signal-to-noise ratio of delay fits. The Stokes RR and LL signals were, however, calibrated independently. The phase

[7] Faint Images of the Radio Sky at Twenty-Centimeters (R. H. Becker et al. 1995).

[8] https://www.aips.nrao.edu/cgi-bin/ZXHLP2.PL?VLBARUN

Table 1
VLBA Observation Details

Source Name	R.A.	Decl.	Date	Sun	Frequency	PhaseCal Name	Separation	No. of Antennas	Epoch-I References
	hh mm ss	deg arcmin arcsec	DD/MM/YY	(deg)	(GHz)		(deg)		
(1)	(2)	(3)	(4)	(5)	(6)	(7)	(8)	(9)	(10)
KISSR102	12 41 35.143	28 50 36.270	15/09/2022	30.7	1.54	1246+285	1.78	8	P. Kharb et al. (2020)
			18/09/2022	30.4	4.98	1246+285		7	
KISSR434	14 03 45.022	29 21 43.980	29/11/2022	60.2	1.54	1404+286	1.15	8	P. Kharb et al. (2019)
			01/09/2022	52.1	4.98	1404+286		9	
KISSR618	15 02 28.776	28 58 15.600	04/09/2022	62.9	1.54	J1454+29	1.98	9	P. Kharb et al. (2021)
KISSR872*	15 50 09.805	29 11 07.230	13/09/2022	67.9	1.54	1537+279	2.72	8	P. Kharb et al. (2021)
			05/11/2022	121.0	4.98	1537+279		9	
KISSR967	16 06 31.602	29 27 56.112	17/09/2022	69.1	1.54	1603+301	0.60	7	P. Kharb et al. (2021)
KISSR1154	11 56 32.871	42 59 39.270	16/09/2022	40.5	1.54	1147+438	1.26	7	P. Kharb et al. (2021)
KISSR1219	12 09 08.809	44 00 11.500	06/11/2022	69.4	1.54	1218+444	2.22	9	P. Kharb et al. (2017b)
KISSR1494	13 13 25.849	43 32 14.790	17/10/2022	52.7	1.54	1325+436	2.53	8	P. Kharb et al. (2015)

Note. Columns (1), (2), and (3): source name and R.A., decl. of the sources. Column (4): date of observation in day, month, and year. Column (5): separation between the source and the Sun in degrees. Columns (6), (7), (8), and (9): the observing frequency in GHz, phase reference calibrator name, its separation from the KISSR source in degrees, and the number of VLBA antennas used in the observations, respectively. Column (10): references for epoch-I observations. ∗Epoch-II results from KISSR872 have been presented in P. Kharb et al. (2024).

solutions were linearly interpolated in time between calibrator scans, with the caveat that this approach may be inappropriate if the phase varies nonlinearly on timescales shorter than the phase-referencing cycle time, particularly due to the proximity of the Sun. Los Alamos (LA) was chosen as the reference antenna for calibrating the various datasets. Data were not flagged, and the phase reference calibrators, chosen as compact sources on VLBI scales, were not self-calibrated during VLBARUN.

Finally, the 64 spectral channels were averaged, and individual sources were "SPLIT" from the multisource data after the application of the calibration tables. We note that these data-reduction steps, as well as the choice of calibrators, were identical to those used in Epoch-I observations.

Imaging was carried out using the AIPS task IMAGR. Natural weighting with a ROBUST parameter of +5 was used for the imaging (Figures 1–9). Due to the radio faintness of the sources, no self-calibration was carried out. The peak intensity and total flux density with errors for compact components like the "core" were estimated using the Gaussian-fitting task JMFIT in AIPS (see Table 2). The final rms noise in the images was obtained using the AIPS verbs TVWIN and IMSTAT. We obtained the total flux density of the extended features (e.g., "C+J," and J1, J2 in Table 2) using the AIPS verb TVSTAT. The error in the total flux density was typically $\leqslant$5%.

We created the 1.5–5 GHz spectral index image for KISSR102 by first making differently weighted images using ROBUST $= -5$ (pure uniform weighting) at 1.5 GHz and ROBUST $= +5$ (natural weighting) at 5 GHz and then convolving both images with a synthesized beam of 9 mas $\times$ 3 mas at PA $= 8°$. The AIPS task COMB was used to create the spectral index image (Figure 1). Pixels with flux density values below 3 times the rms noise were blanked using COMB. A spectral index noise image was created as well.

4. VLA Observations

Observations were also carried out for four KISSR sources, viz. KISSR434, KISSR618, KISSR872, and KISSR967 on 2021 February 23 at 1.5 GHz with the Karl G. Jansky Very Large Array (VLA) in the A-array configuration, with a bandwidth of 1 GHz. The remaining four sources could not be observed due to the low scheduling priority of the project; data from these sources will be acquired in the near future. For the VLA experiment, 3C286 was used as the flux density and polarization angle calibrator while the unpolarized source J1407+2827 was used as the polarization leakage calibrator. J1407+2827 was used as the phase calibrator for KISSR434, J1513+2338 for KISSR618, and J1609+2641 for KISSR872 and KISSR967, respectively.

Each source was observed for $\sim$15 minutes. The initial calibration on the data was performed by using the CASA-based automated VLA pipeline which includes flagging, and initial bandpass and gain calibrations. We performed additional flagging, final gain calibration, and polarization calibration following standard procedures. The calibrated visibility data for the sources were then SPLIT and fast Fourier transformed using the tclean task in CASA with the Multi-term Multi-frequency Synthesis (MTMFS) deconvolution algorithm, and a Briggs' weighting with ROBUST parameter of +0.5 (ROBUST 0 for KISSR434). We performed self-calibration on KISSR434 and KISSR967 with three rounds of phase-only and two rounds of amplitude+phase calibration. For KISSR618 and KISSR872, self-calibration could not be carried out due to too many failed solutions because of the faintness of the sources. The resultant Stokes I, Q, U images were used to make the total intensity, linear polarization, and fractional polarization images (see Figures 10–12).

As the MTMFS algorithm was used with nterms=2, we also obtained the spectral index and error images. The task COMB was used for creating the polarization images by blanking pixels with less than 3σ signal in Stokes Q and U images, and errors greater than 10° in the polarization angle image. The fractional polarization was created after blanking pixels with greater than 20% error in fractional polarization. The spectral index images presented in Figure 10 were created after using spectral index noise images and blanking errors greater than 0.5, 0.2, 0.5, and 0.3 for KISSR434, KISSR872, KISSR618, and KISSR967, respectively. Pixels with flux density values below 3 times the rms noise in the total intensity image were also blanked using the task COMB.

5. Results

The VLBA detected parsec-scale emission at 1.5 GHz in seven out of the eight KISSR sources in these second-epoch observations (see Figures 1 to 9). All labeled features are at the $>5\sigma$ significance level. However, in sources like KISSR1494 (Figure 8), the lowest contour is chosen to be $\approx 2\sigma$ to primarily highlight the diffuse emission (around component J1). KISSR967, which was detected at the $\sim 5\sigma$ level with a total flux density of $\sim$160 μJy at 1.5 GHz in 2019 January is not detected $\sim$3.7 yr later. For this source image, the rms noise is higher in epoch-II compared to epoch-I by a factor of 1.2–1.4. However, the drop in core flux density (assuming 3σ as an upper limit to core flux density in epoch-II) between the two epochs is $\sim$27%. The nondetection of emission from KISSR967 could therefore be related to intrinsic source variability.

Table 3 lists the "core" flux density changes that occurred within the time interval between the two epochs. The largest changes in "core" flux density are observed in the case of KISSR872 (39% $\pm$ 6%) and KISSR102 (29% $\pm$ 7%) in a time period of 3.66 and 3.69 yr, respectively (see Section 5.3). Interestingly, these two LINER galaxies are also the two sources showing the presence of superluminal jet motion. For the remaining sources, the "core" flux density changes are not significant. We discuss changes in jet morphology and spectral indices between the two observation epochs, below.

5.1. VLBI "Cores" and Gaia Optical Positions

Our assumption of the brightest feature being the radio "core" seems largely to be validated in these KISSR galaxies. With the exception of KISSR872 and KISSR618, the highest intensity features are also the "stationary" features. We have included the Gaia DR3 optical positions of the centers of the host galaxies in Figures 1–9. With the exception of KISSR102, the VLBI "cores" in all sources are offset by 21 to 169 mas (see Table 3). However, this offset may be understood as large astrometric uncertainties in the optical positions. For instance, the *astrometric_excess_noise* parameter, which is the extra noise that is needed per observation to explain the scatter of residuals in the astrometric solutions (L. Lindegren et al. 2021), is large for the KISSR galaxies ($\sim$5–33 mas). Another

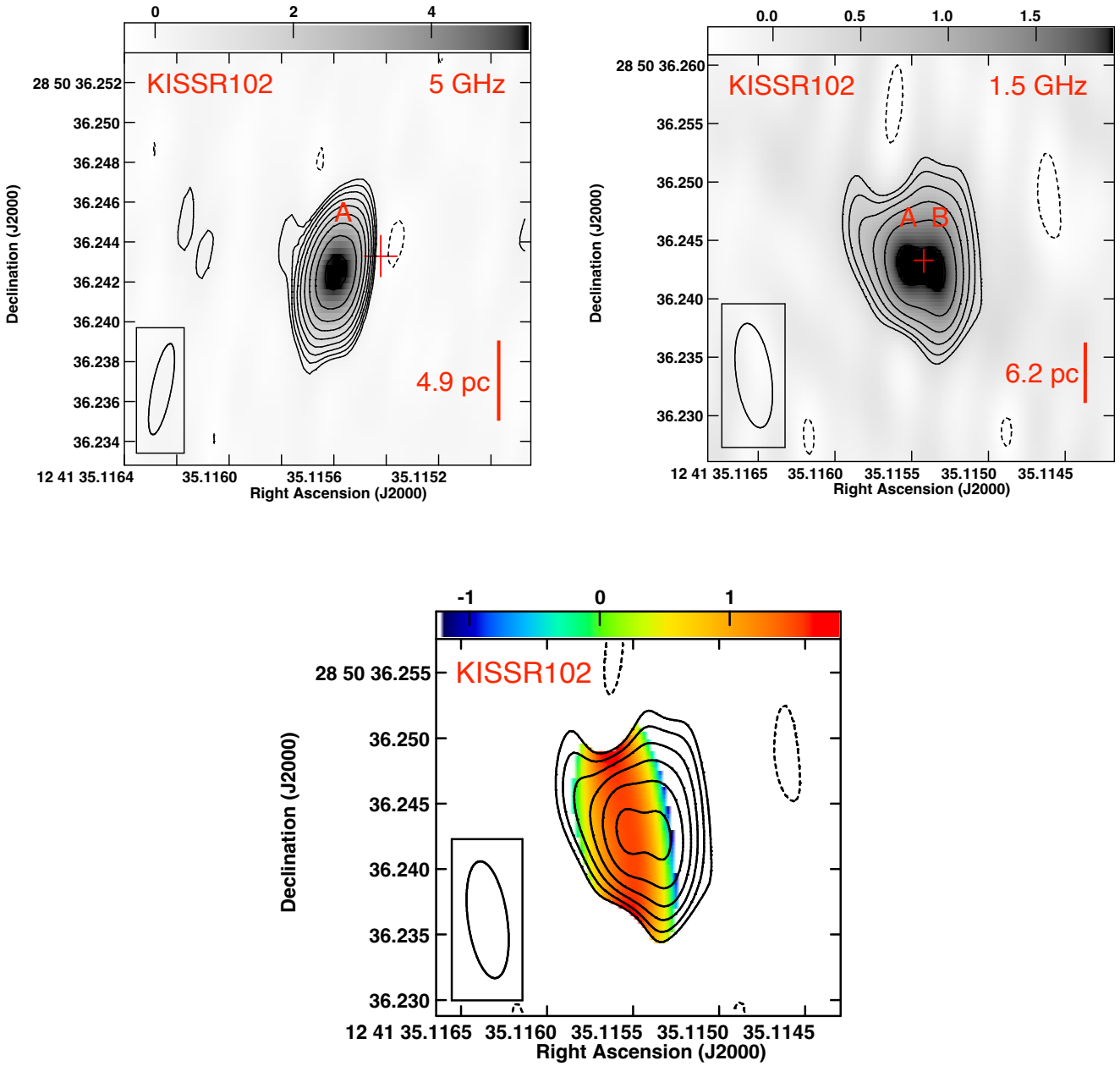

Figure 1. (Top left) 5 GHz VLBA image of KISSR102. The grayscale varies from −0.36 to 5.35 mJy beam^{-1}. The contour levels are 59.17 × (± 5.6, 11.3, 22.5, 45, 90) μJy beam^{-1}. The beam is of size 4.6 × 0.96 mas at PA = −11.°2. (Top right) 1.5 GHz VLBA image of KISSR102. The grayscale varies from −0.32 to 1.82 mJy beam^{-1}. The contour levels are 20.26 × (± 16, 22.5, 32, 45, 64, 90) μJy beam^{-1}. The beam is of size 8.4 × 2.8 mas at PA = 4.°4. In both the panels, the cross symbol denotes the Gaia position of the galaxy: R.A. 190.°396314252, decl. 28.°843400915 with respective errors of 1.03 and 0.82 mas. The size of the cross is 2 times the positional uncertainty noted here. (Bottom) 1.5–5 GHz spectral index image in color superimposed by 1.5 GHz contours. The contour levels are 21.27 × (± 16, 22.5, 32, 45, 64, 90) μJy beam^{-1}. The beam is of size 9 × 3 mas at PA = 8°.

goodness-of-fit parameter is the renormalized unit weight error (ruwe; L. Lindegren et al. 2018). This parameter is expected to be close to 1.0 for well behaved sources, and has been estimated in Gaia DR3 only for KISSR102 (ruwe = 1.87), KISSR872 (ruwe = 3.23), and KISSR1494 (ruwe = 1.74), suggesting a relatively poor astrometric fit. Consistent with this suggestion, we find that the largest offsets between the VLBI "core" and the Gaia positions are in KISSR434, KISSR1154, and KISSR1494, respectively, which are inclined spiral galaxies with prominent spiral arms and dust lanes. The presence of the extended light from the galactic bulge, dust lanes, and circumnuclear star clusters, can shift the optical centroid away from the SMBH. The weakness and the variability of the optical AGN emission can be an additional contributor to astrometric uncertainties in the KISSR galaxies.

5.2. Global Properties of the KISSR Galaxies

We list some of the global properties of the sample sources in Table 4. The 6 GHz radio luminosity, L_6, was estimated by extrapolating the integrated flux density at 1.4 GHz from the VLA FIRST survey with a global spectral index of −0.7. All the sample sources satisfy the "radio-quiet" classification as defined by K. I. Kellermann et al. (2016), i.e., they have $10^{21} \lesssim L_6 \lesssim 10^{23.2}$ W Hz^{-1}. The time-averaged kinetic jet power of the radio outflows in the KISSR sources was

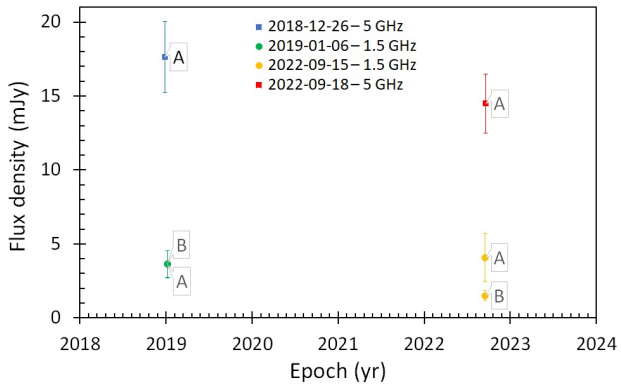

Figure 2. The flux density of the components detected in the radio images of KISSR102 at 1.54 GHz (green and orange circles) and 4.98 GHz (blue and red squares). Component A is the core region of KISSR102, and B is the jet component.

estimated following the relations used for "radio-loud" AGN (see B. Punsly & S. Zhang 2011). We derived the flux density at 151 MHz, F_{151}, that is needed for the calculation, using the 1.4 GHz flux density from the kiloparsec-scale FIRST images and a jet/lobe spectral index of −0.7. The star formation rate (SFR) is derived from the Hα narrow-line luminosity and the R. C. Kennicutt (1998) relation, while the black hole mass is based on the M–$\sigma_\star$ relation (N. J. McConnell & C.-P. Ma 2013). The bolometric luminosity, L_{bol}, is based on the [O III] line luminosity and the scaling relation from T. M. Heckman et al. (2004). We see that the L_{bol} for the sources range between 10^{43} and 10^{44} erg s^{-1}; the Seyfert galaxies in this sample therefore have low luminosities similar to the LINER galaxies, which typically have $L_{bol} \leqslant 10^{43}$ erg s^{-1} (e.g., G. Younes et al. 2012; L. Spinoglio et al. 2024).

5.3. VLBI Features between Epochs: Changes in Flux Density, Spectral Index, and Jet Directions

Overall in the second epoch of observations, we find a persistence of the weak radio features that were observed in the first epoch observations, attesting to their reality. Except for KISSR102, we did not detect flat or inverted spectral index "cores" that are consistent with synchrotron self-absorbed bases of jets. Instead, we had identified the "cores" to be the brightest centrally peaked features. These second-epoch phase-referenced observations have largely confirmed that these "cores" are indeed "stationary" features, validating our assumptions. The "core" position remains the same to within 1 mas in a majority of the sources; the peak intensity positions primarily shift by 2.0 mas and 2.9 mas in KISSR618 and KISSR872, respectively. These two sources also show the most variation in its jet base over the two epochs. However, considering the limited astrometric precision and the availability of only two epochs of data, the "cores" may ideally be regarded as "candidate cores." In principle, extremely high-precision differential astrometry (e.g., X. Cheng et al. 2023) is required to confirm their stationarity.

The candidate cores in several sources, viz. KISSR434, KISSR618, KISSR872, and KISSR1494, show associated diffuse emission in a transverse direction. For KISSR618, the broadening of the jet occurs 10 mas from the "core." The width of these jet bases are respectively, 2.4, 1.9, 1.9, and 1.9 times the major axes of their synthesized beams. It is not yet clear if

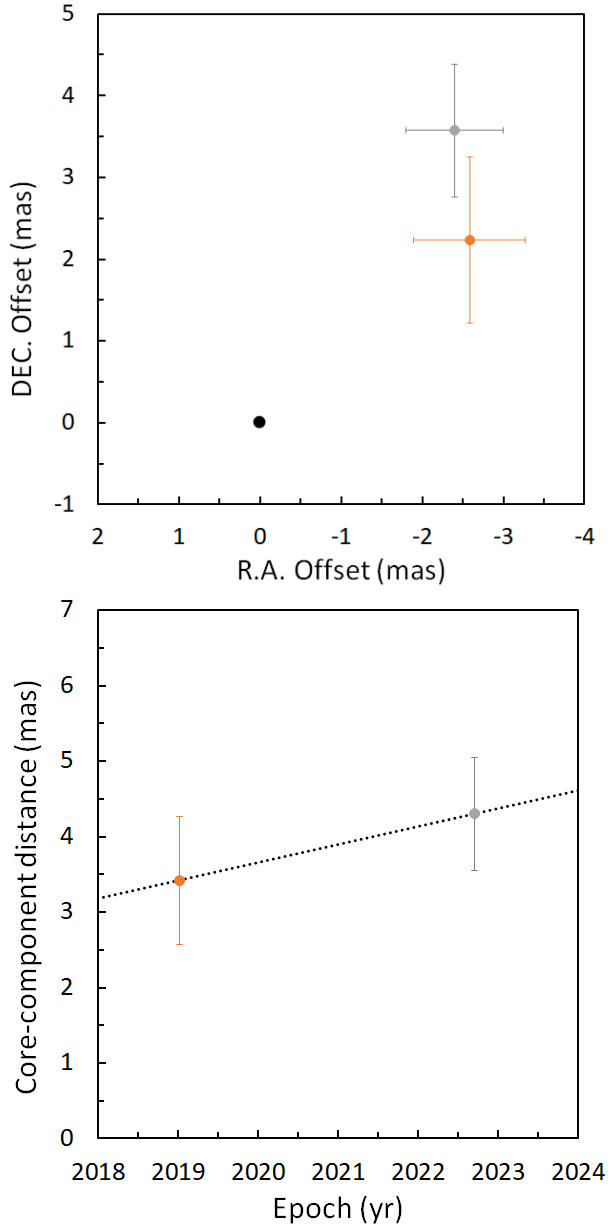

Figure 3. (Top panel) Offsets in R.A. and decl. of the jet component B in KISSR102 in 2019 and 2022 (orange and gray points, respectively) in relation to the core (component A), marked by the black circle. (Bottom panel) The angular distance between A and B in the same two epochs. The dotted line refers to a proper motion of 0.24 mas yr^{-1} (apparent speed of 1.05c).

these structures are similar to the broad base observed in say, the RadioAstron image of 3C84 (G. Giovannini et al. 2018). Their presence will need to be confirmed in future observations of the sample. We discuss this more in Section 6.

It is unclear whether there is a jet in the epoch-II image of KISSR1154. The presence of a weak jet was indicated in this source in the epoch-I data (P. Kharb et al. 2021), attesting to the rapid changes in the jet structures in these sources. Epoch-I observations of KISSR1494 had detected only a candidate core (P. Kharb et al. 2015); however, a jet is clearly detected in epoch-II observations, 9.2 yr later. As the change in sensitivity is not significant between the two epochs (see Table 4) the jet features appear to have significantly brightened over the last 9.2 yr.

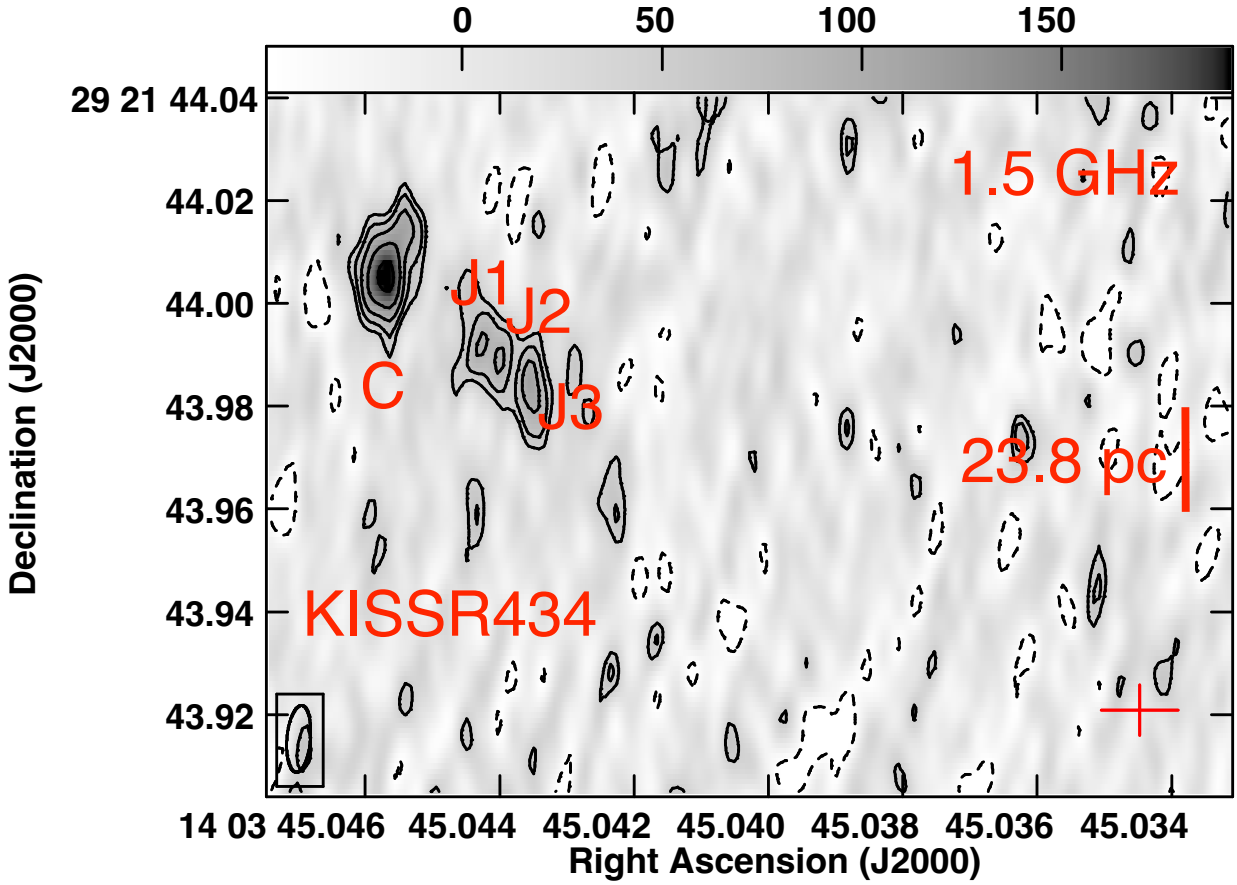

Figure 4. 1.5 GHz VLBA image of KISSR434. The grayscale varies from −47.7 to 191.5 μJy beam^{-1}. The contour levels are 2.12 × (± 22.5, 32, 45, 64, 90) μJy beam^{-1}. The beam is of size 13.03 × 4.57 mas at PA = −4.°9. The cross symbol denotes the Gaia position of the galaxy: R.A. 210.°937643641, decl. 29.°362200227 with respective errors of 1.96 and 2.99 mas. The size of the cross symbol is 5 times this positional uncertainty.

Significant "core" flux density change is observed in KISSR102 (29% ± 7%) and KISSR872 (39% ± 6%). These two sources also exhibit superluminal motion in their jets (see Table 3). The "core" flux density change is not significant in the remaining sources. The flux density change error has been estimated using the rules of error propagation: $100 \times \sqrt{\left(\frac{S_2\,\sigma_{S1}}{S_1^2}\right)^2 + \left(\frac{\sigma_{S2}}{S_1}\right)^2}$, where $\sigma_{S1} = \sqrt{\mathrm{rms}_1^2 + (0.05\,S_1)^2}$ and $\sigma_{S2} = \sqrt{\mathrm{rms}_2^2 + (0.05\,S_2)^2}$, "rms" being the rms noise levels in the respective images and the flux-density-scale error for the VLBA assumed to be 5%.

Of the three sources that were observed at 5 GHz in epoch-II, only two sources, viz. KISSR102 and KISSR872, were detected at 5 GHz. KISSR434 was not detected at 5 GHz in this second epoch; in the previous epoch, this source had exhibited steep-spectrum emission ($\alpha = -0.9$ to -1.3) in its candidate core region (P. Kharb et al. 2019). The "core" spectral index in KISSR102 changed from +0.64 ± 0.08 in epoch-I to +0.91 ± 0.13 in epoch-II, 3.7 yr later. This source is discussed in greater detail in Section 5.4.1. The flattening of the 1.5–5 GHz spectral index from −0.71 ± 0.26 to −0.31 ± 0.19 for the core-jet region in KISSR872 has already been discussed in P. Kharb et al. (2024). Therefore, both the jet structures and jet spectral indices vary between epochs.

We had fitted a precessing jet model to the curved jet KISSR434 in P. Kharb et al. (2019). The curved jet in KISSR434 continues to remain curved 4 yr later. The persistence of the curvature disfavors the jet nozzle precession model but supports the idea that the jet plasma is flowing along a curved path. In KISSR618, the parsec-scale jet has changed its direction of propagation by nearly 30°. There also appears to be flaring in the inner jet around 10 mas from the core. However, overall there remains some extended emission in the previously observed jet direction.

5.4. Estimating Jet Speeds in KISSR Sources

A comparison of the jet knot positions in two of the LINER galaxies, viz., KISSR872 and KISSR102, indicates the presence of relativistic jet motion. As far as we are aware, this makes KISSR872 and KISSR102 the only two radio-quiet LINER galaxies to reveal relativistic or superluminal motion in their parsec-scale jets. A jet knot is seen to move at a speed of 1.65 ± 0.57c in ∼4 yr in KISSR872 (P. Kharb et al. 2024). KISSR102 showed the presence of two compact radio cores in the image from 2018 December 26 (P. Kharb et al. 2020) but now reveals superluminal jet motion (see Section 5.4.1). Recently, A. Wang et al. (2025) have detected superluminal jet motion ($\beta_{\rm app}$ = 1.5–3.6) in the "radio-quiet" narrow-line Seyfert 1 galaxy, Mrk110.

So far, we have closely examined two of the seven sources with the simplest core-jet structures. More sophisticated methods like those discussed in Section 5.4.1 will need to be employed for the other sources that show jet features that are not compact making them difficult to identify and trace (e.g., KISSR434). The jet components observed in epoch-I 7.75 yr ago in KISSR1219 appear to have moved away. If indeed J1

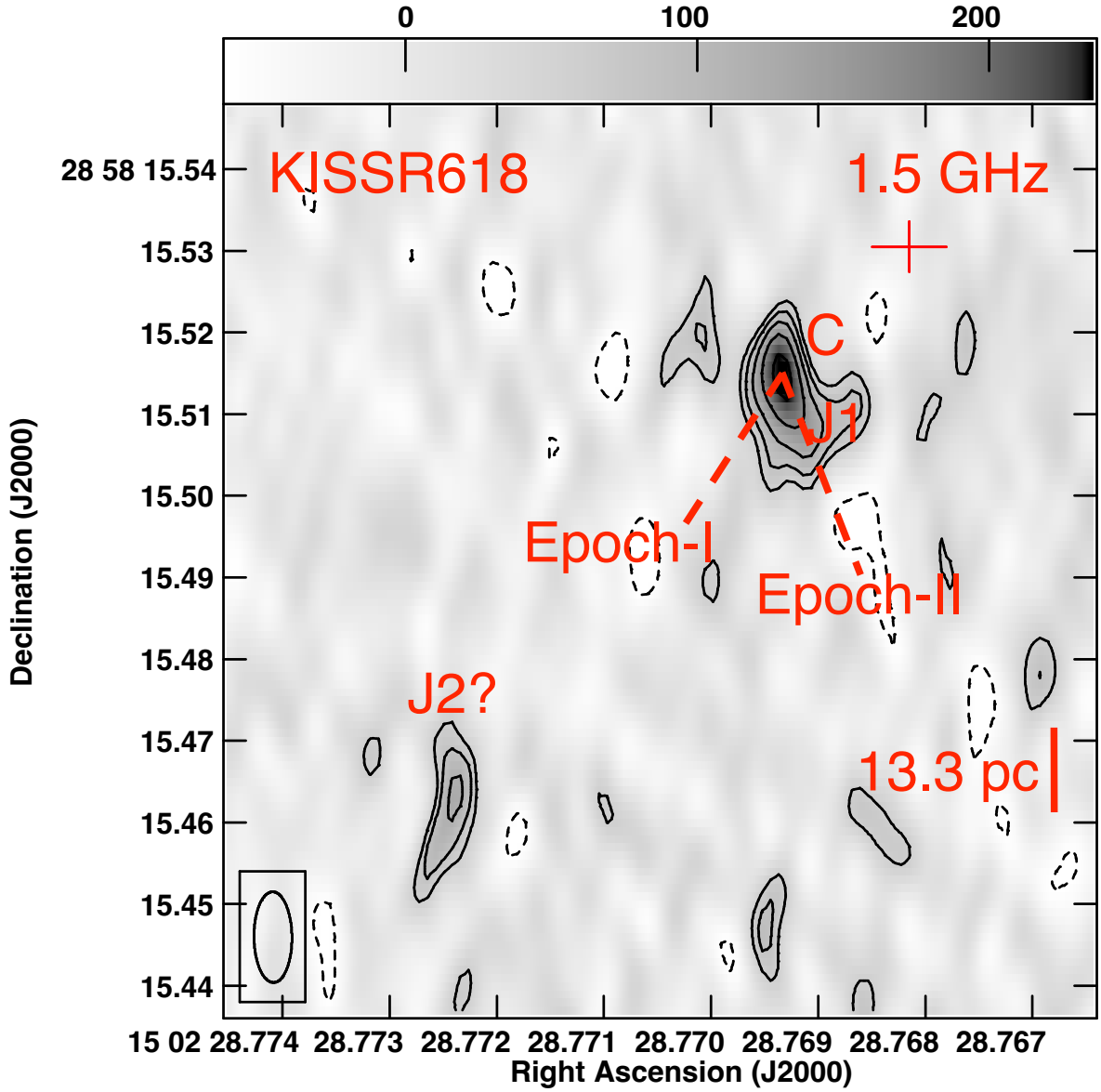

Figure 5. 1.5 GHz VLBA image of KISSR618. The grayscale varies from −59.6 to 234.2 μJy beam^{-1}. The contour levels are 2.59 × (± 22.5, 32, 45, 64, 90) μJy beam^{-1}. The beam is of size 11.11 × 4.65 mas at PA = 0.°6. The cross symbol denotes the Gaia position of the galaxy: R.A. 225.°619867285, decl. 28.°970980695 with respective errors of 1.23 mas and 1.82 mas. The size of the cross symbol is 5 times this positional uncertainty.

and J2 (see Figure 7) are the same components as seen in epoch-I for KISSR1219, the apparent jet speed is 2.42 and 0.88 c, respectively. VLBI monitoring is therefore required to confirm the jet speeds in KISSR1219 and other sources.

5.4.1. A Relativistic Jet in KISSR102

We used the cross-entropy (CE) global optimization technique (R. Y. Rubinstein 1997) to model our four VLBI images of KISSR102. The CE optimization was originally adapted by A. Caproni et al. (2011) to deal with the problem of discretizing interferometric radio images in terms of two-dimensional elliptical Gaussian components, having been applied to other jetted radio sources in former works (A. Caproni et al. 2014, 2017; V. Y. D. Sumida et al. 2021; S. Nandi et al. 2024). Each elliptical Gaussian has six free parameters to be determined: peak intensity, I_0, two-dimensional peak position (x_0, y_0), with the coordinates x and y oriented, respectively, to R.A. and decl. directions, semimajor axis, a, eccentricity, $\epsilon = \sqrt{1-(b/a)^2}$, where b is the semiminor axis, and the position angle of the major axis, ψ, measured positively from west to north.

In short, CE optimization tests each tentative solution involving the combination of N_c elliptical Gaussian components against a predefined merit function. It considers the 20 solutions with the lowest merit function values to build the next sample of tentative solutions (e.g., see A. Caproni et al. 2014 for more details). The CE optimization is halted when either the maximum number of iterations is reached or the rms value of the associated residual image falls below the nominal rms value provided in Table 2. This process is repeated twice for each interferometric image, selecting the CE optimization that best minimizes the merit function for determining the structural parameters of the Gaussian components and their respective uncertainties (see A. Caproni et al. 2011 for more details).

Using the criteria proposed by A. Caproni et al. (2014), we determined the optimal number of elliptical Gaussian components

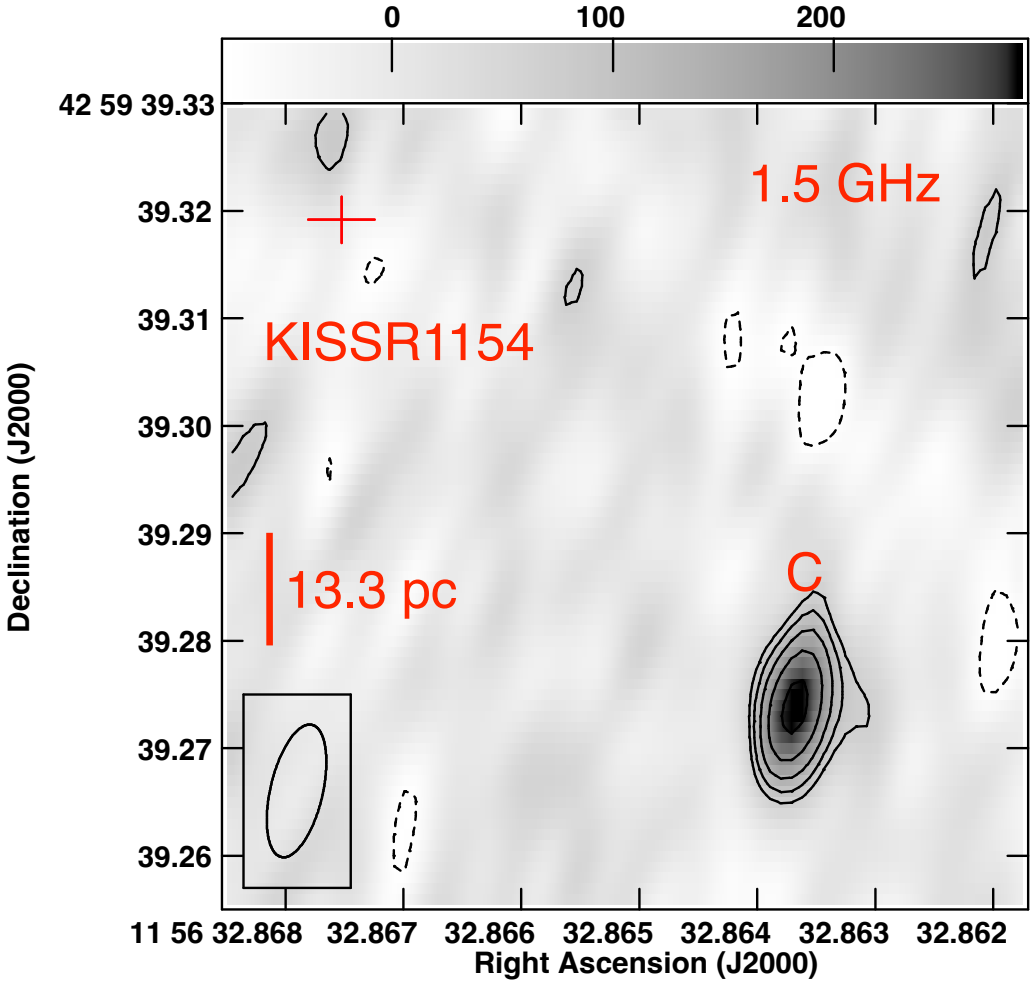

Figure 6. 1.5 GHz VLBA image of KISSR1154. The grayscale varies from −70.4 to 281.7 μJy beam^{-1}. The contour levels are 3.13 × (± 22.5, 32, 45, 64, 90) μJy beam^{-1}. The beam is of size 12.62 × 4.87 mas at PA = −13.°1. The cross symbol denotes the Gaia position of the galaxy: R.A. 179.°136948020, decl. 42.°994255321 with respective errors of 4.36 mas and 6.19 mas. The size of the cross symbol represents this positional uncertainty.

in each of the four VLBI images of KISSR102. For the two radio maps at 4.98 GHz, one single Gaussian component is enough to represent the brightness distribution of KISSR102, while two Gaussian components were necessary to provide a fair description of the two 1.54 GHz images. We show in Figure 2 the time behavior of the flux density of the Gaussian components A and B for the two epochs analyzed in this work. Both components show changes in their flux densities between ∼2019 and 2022.7. Component A becomes slightly fainter at 4.98 GHz and brighter at 1.54 GHz, while component B decreases its flux density at 1.54 GHz. Comparing the flux densities of the component A at 1.54 and 4.98 GHz, we obtained $\alpha \sim 1.4$ in 2019 and $\alpha \sim 1.1$ in 2022.7, implying that A is optically thick in both epochs. These findings are in agreement with the spectral index map of KISSR102 shown in the bottom panel of Figure 1, suggesting that A is likely the core region of KISSR102 and B is a jet component.

In the top panel of Figure 3, we show the offsets in R.A. and decl. of component B relative to core A at 1.54 GHz, while its core-component separation is presented in the bottom panel. Between ∼2019 and 2022.7, component B has receded from A at a mean position angle around −42° and with a proper motion of 0.24 ± 0.10 mas yr^{-1}, which translates to an apparent speed of (1.05 ± 0.45)c. Superluminal motions are commonly reported in blazars but not in LINERS, for which KISSR872 is the only documented case in the literature (P. Kharb et al. 2024).

Interestingly, the mean position angle of component B (−42°) agrees with the position angle of the secondary optical nucleus N2 seen in SDSS images of KISSR102 (see Figure 1 in P. Kharb et al. 2020). It suggests an alternative interpretation for N2 in which it would be a kiloparsec-scale jet component ejected from N1 ∼5000 yr ago (considering that N2 has the same proper motion as the parsec-scale jet component B). This possibility could also explain the poor modeling obtained by P. Kharb et al. (2020) after assuming N2 as a point source since jet components are expected to expand as they recede from the core region. This interpretation also suggests a possible interaction between the jet and the interstellar medium ("AGN feedback"), which would be in full agreement with optical forbidden emission lines being excited by shocks in the case of KISSR102 (P. Kharb et al. 2020). Higher resolution VLA images will be required to confirm this hypothesis.

The bulk speed of the jet in terms of c, β, and the viewing angle of the jet, ϕ, can be determined univocally from the

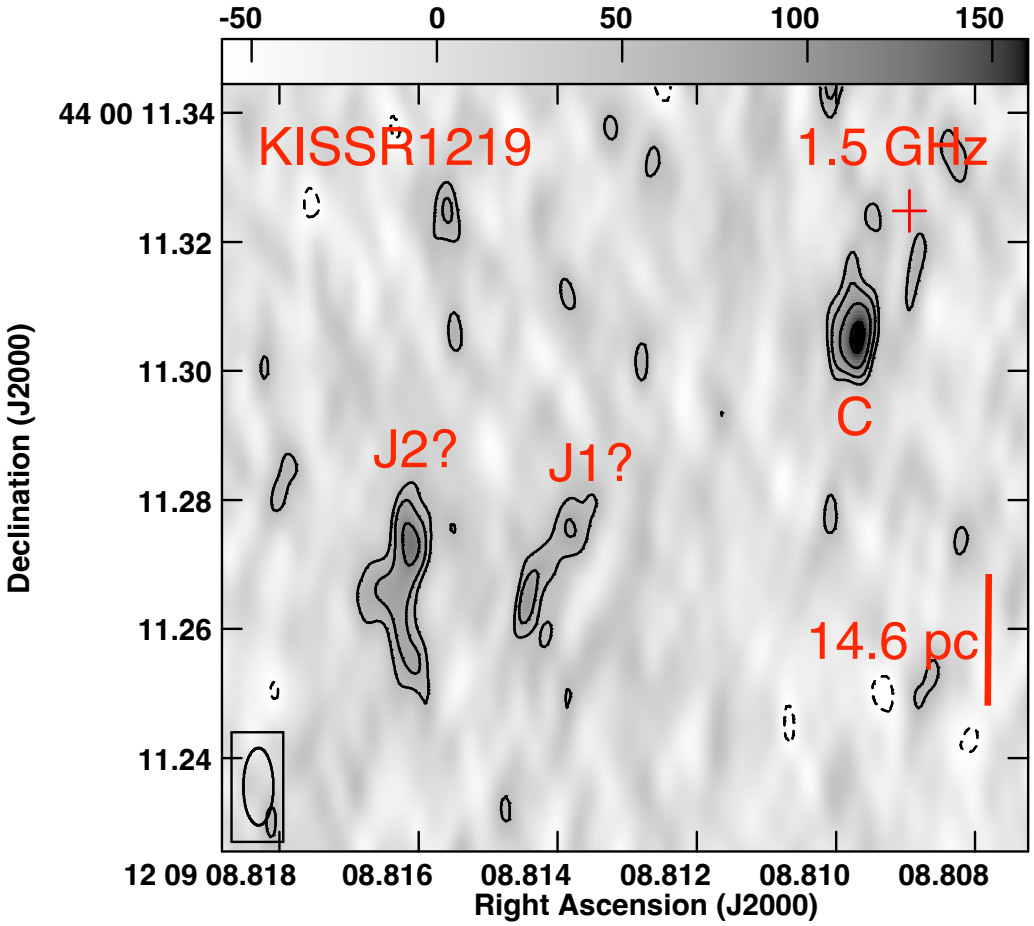

Figure 7. 1.5 GHz VLBA image of KISSR1219. The grayscale varies from −56.0 to 157.5 μJy beam^{-1}. The contour levels are 1.75 × (± 32, 45, 64, 90) μJy beam^{-1}. The beam is of size 11.98 × 4.65 mas at PA = 0.°1. The cross symbol denotes the Gaia position of the galaxy: R.A. 182.°286703941, decl. 44.°003145789 with respective errors of 0.64 mas and 0.50 mas. The size of the cross symbol is 10 times this positional uncertainty.

apparent speed of the jet, $\beta_{\rm app}$, defined as

$$\beta_{\rm app} = \frac{\beta \sin\phi}{(1 - \beta\cos\phi)}, \quad (1)$$

and the measured flux densities at a frequency ν for the jet, $S_{\nu,\rm j}$, and counterjet, $S_{\nu,\rm cj}$. Assuming the flux densities of the jet and counterjet in the source's reference frame are equal, any difference between $S_{\nu,\rm j}$ and $S_{\nu,\rm cj}$ is due to the relativistic Doppler boosting effect, so that for a continuous jet (e.g., K. R. Lind & R. D. Blandford 1985)

$$\frac{S_{\nu,\rm j}}{S_{\nu,\rm cj}} = \left(\frac{1 + \beta\cos\phi}{1 - \beta\cos\phi}\right)^{2-\alpha}. \quad (2)$$

Thus, using $\beta_{\rm app}$ (=1.05c) of the jet component B estimated in this work, together with $S_{\nu,\rm j}/S_{\nu,\rm cj} \approx 20$ and $\alpha = -1.6$ (P. Kharb et al. 2020), we derived $\beta \approx 0.75c$ and $\phi \approx 58°$ for the pc-scale jet of KISSR102.

These values allow a rough estimation of the maximum projected distance from A that the counterjet has reached in the last 5000 yr. Assuming that jet components are ejected from the core at 0.75c at a viewing angle of 58°, maintaining both values during their displacements, the counterjet must have extended to an angular distance of about 0.″5 from A. It corresponds to twice the pixel size of the i-band image of KISSR102 shown in the left panel of Figure 4 in P. Kharb et al. (2020). Therefore, a possible interaction between the counterjet and the interstellar medium that could be detected at optical wavelengths would be barely resolved in the referred i-band image of KISSR102. However, the excess seen in the residual map close to the location of N1 (right panel in Figure 4 of P. Kharb et al. 2020) might indicate underlying diffuse emission that could be due to the counterjet itself.

5.5. Extended Radio Emission in the VLA Images

While jets are not observed in the VLA images, extended (extranuclear) emission is detected in all four sources (Figure 10), the morphology of which is typically core-lobe-like[9] (in KISSR434, KISSR872, and KISSR967) or core-halo-like[10] (in KISSR618). The extension in KISSR967 is, however, along the direction of the second optical nucleus observed in this galaxy.

The in-band spectral indices shown in Figure 10 reveal an average spectral index ranging from −0.7 ± 0.3 to −0.90 ± 0.06, consistent with synchrotron emission. Spectral index gradients are observed in all four sources. These gradients may be hinting at the directions of unresolved jetted structures, with the nuclei having a flatter spectrum and the jets having a steeper spectrum. We find that the VLBI jet directions

[9] The diffuse emission shows a directionality.
[10] The diffuse emission is symmetrically distributed around the core.

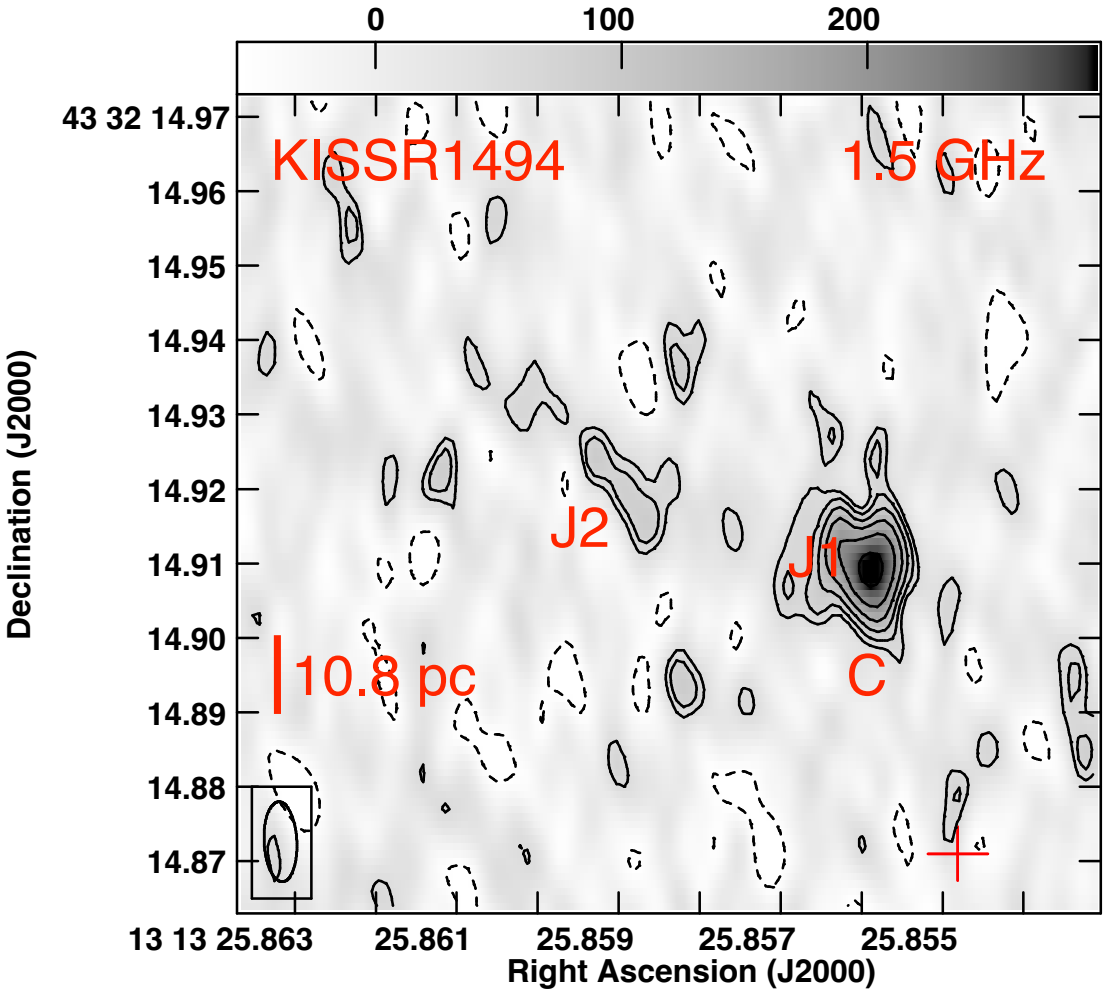

Figure 8. 1.5 GHz VLBA image of KISSR1494. The grayscale varies from −53.3 to 291.8 μJy beam^{-1}. The contour levels are 3.22 × (± 16, 22.5, 32, 45, 64, 90) μJy beam^{-1}. The beam is of size 10.75 × 4.40 mas at PA = 2.°8. The cross symbol denotes the Gaia position of the galaxy: R.A. 198.°357728378, decl. 43.°537464172 with respective errors of 0.36 mas and 0.40 mas. The size of the cross symbol is 10 times this positional uncertainty.

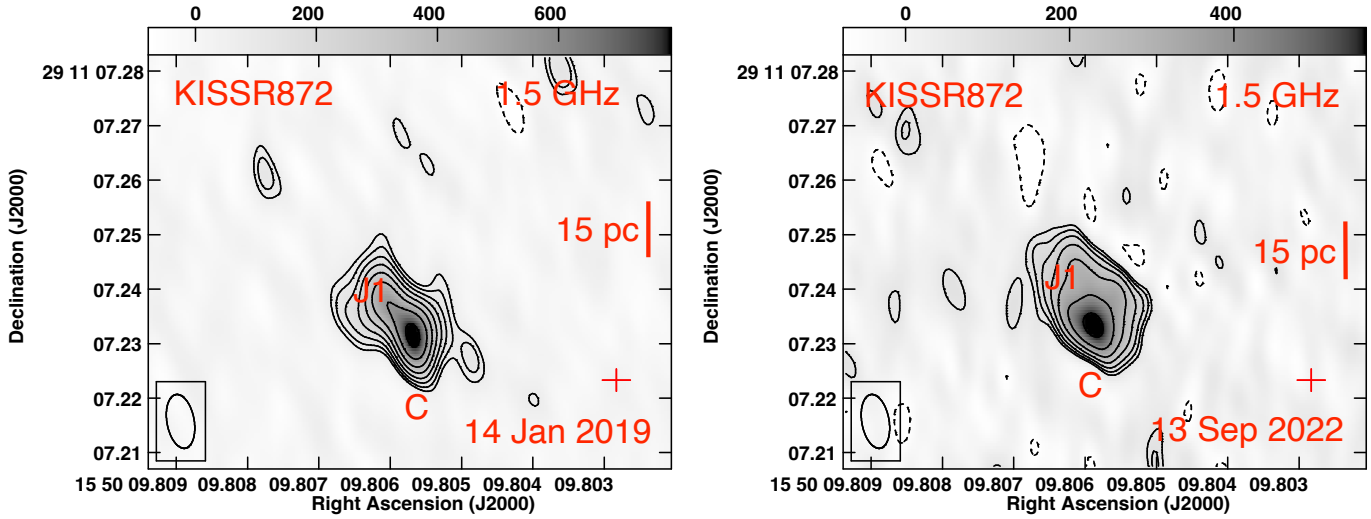

Figure 9. 1.5 GHz VLBA image of KISSR872 (left) from Epoch-I, 14 January 2019, and (right) from Epoch-II, 2022 September 13. The grayscale varies from (left) −73.3 to 781.7 μJy beam^{-1}, and (right) −72.8 to 558.0 μJy beam^{-1}. The contour levels are (left) 8.64 × (± 8, 11.3, 16, 22.5, 32, 45, 64, 90) μJy beam^{-1}, and (right) 6.17 × (± 11.3, 16, 22.5, 32, 45, 64, 90) μJy beam^{-1}. The beam is of size 10 × 5 mas at PA = 10° in both the panels. The cross symbol denotes the Gaia position of the galaxy: R.A. 237.°540845128, decl. 29.°185339806 with respective errors of 0.41 mas and 0.51 mas. The size of the cross symbol is 10 times this positional uncertainty.

Table 2
Results from the VLBA Observations

Source Name and Freq. Band	z	Type	Component	I_{peak} (μJy beam^{-1})	S_{total} (μJy)	rms (μJy beam^{-1})	Scale (pc/mas)	Extent (mas)	Extent (pc)
(1)	(2)	(3)	(4)	(5)	(6)	(7)	(8)	(9)	(10)
KISSR102 *L*-band	0.066320	LINER	A	1924 ± 98	2538 ± 204	100.6	1.237	4.30	5.40
…	…	…	B	1697 ± 97	2408 ± 214	…	…	…	…
KISSR102 *C*-band	…	…	A	6250 ± 64	13880 ± 197	75.65	…	…	…
KISSR434 *L*-band	0.064128	Sy 2	C	208 ± 26	475 ± 80	24.00	1.189	66.48	79.04
…	…	…	C+J	…	497	…	…	…	…
…	…	…	J1+J2+J3	…	573	…	…	…	…
KISSR434 *C*-band	…	…	N	…	…	21.14	…	…	…
KISSR618 *L*-band	0.072940	Sy 2	C	254 ± 25	435 ± 63	25.13	1.332	77.95	103.83
…	…	…	C+J1	…	510	…	…	…	…
…	…	…	J2	…	200	…	…	…	…
KISSR872[a] *L*-band	0.083064	LINER	C+J1	475 ± 27	1601 ± 116	29.54	1.497	…	…
KISSR872[a] *C*-band	…	…	C	334 ± 22	472 ± 49	18.50	…	…	…
KISSR967 *L*-band	0.092067	LINER	N	…	…	36.98	1.648	…	…
KISSR1154 *L*-band	0.072032	Sy 2	C	313 ± 33	385 ± 66	31.81	1.329	…	…
…	…	…	C+J	…	387	…	…	…	…
KISSR1219 *L*-band	0.037580	Sy 2	C	168 ± 24	252 ± 56	23.89	0.729	89.98	65.60
…	…	…	C+J	…	267	…	…	…	…
…	…	…	J1	…	235	…	…	…	…
…	…	…	J2	…	389	…	…	…	…
KISSR1494 *L*-band	0.057446	Sy 2	C	321 ± 27	691 ± 81	29.92	1.082	60.82	65.81
…	…	…	C+J1	…	837	…	…	…	…
…	…	…	J2	…	180	…	…	…	…

Note.
[a] Results for KISSR872 have been presented in P. Kharb et al. (2024); in this paper, we reproduce the *L*-band images of KISSR872 for both epochs to highlight the changes in its jet base. Column (1): source name and observing frequency, *L*-band at 1.54 GHz, and *C*-band at 4.98 GHz. Column (2): redshift. Column (3): AGN classification. Column (4): core (C), core+jet (C+J), individual jet components (J1, J2), N = no detection. "C+J" or "C+J1" denote the "core" along with unresolved jet emission. For KISSR102, components A and B are as shown in Figure 1. Columns (5) and (6): the peak intensity and total flux density. For the candidate cores, these were estimated using the AIPS Gaussian-fitting task JMFIT. The total flux density for C+J and other extended jet features were estimated using the AIPS verb TVSTAT, with the error typically being $\leqslant$5%. Column (7): the final rms noise in the image. Column (8): spatial scale in parsecs corresponding to 1 mas angular scale at the source distance. Columns (9) and (10): total extent of the radio (jet) emission in milliarcseconds and parsecs, respectively.

are aligned with the spectral index gradients in all four sources. This strongly supports an AGN-jet-related origin for the VLA-scale emission.

Moreover, if we assume that all of the observed radio luminosity is attributable to star formation, an SFR can be derived using the relations in J. J. Condon (1992, Equation (21)). We have derived these SFRs for stellar masses $\geqslant 5\,M_{\odot}$ (SFR1) and for stellar masses $M \geqslant 0.1\,M_{\odot}$ (SFR2) in Table 5. SFR2 is $\approx$5.5 times SFR1 (J. J. Condon et al. 2002). For these calculations, we have subtracted the peak flux density of the radio emission, which is associated with the AGN itself, from the total radio flux density. The average spectral index used for the estimation is noted in Table 5. A comparison with the SFR derived from the Hα emission lines in Table 4 shows that the SFR ($M \geqslant 5\,M_{\odot}$) derived from the radio emission is between 5 and 25 times larger (these extreme values are for KISSR872 and KISSR618, respectively). For stellar masses $M \geqslant 0.1\,M_{\odot}$, these values differ by factors ranging from 28 to 136 (for KISSR872 and KISSR618, respectively) with the radio SFR therefore being 2–3 orders higher than the Hα derived SFR. We conclude that the extended radio emission observed in the VLA images is likely to be AGN-related rather than stellar or supernovae-related.

Polarization is detected at the edge of the lobe in KISSR872 (Figure 11). The fractional polarization is 28% ± 9% at a polarization angle of 14° ± 8°. None of the other three sources reveal any polarization. Interestingly, the detected polarization in KISSR872 is in the direction of the secondary nucleus in this interacting galaxy. The SDSS image of KISSR872 reveals not only the tidal tail to the southeast of the primary nucleus but also a faint tail toward the north, in between the two optical nuclei, in fact just north of the detected polarization. We discuss a possible interpretation in Section 6.

Ascribing the extended radio emission seen in the VLA images for the four KISSR sources to the AGN implies that already at the $\sim$1″ scales (typical FWHM of the VLA synthesized beam at this frequency), which corresponds to spatial scales of 1.0–1.5 kpc-scale for these sources, the jets in these sources have lost collimation or "flared" into radio lobes. As the largest "jets" that we have observed in our VLBA observations (e.g., P. Kharb et al. 2019, 2021) were of 100–200 pc extents, the jet decollimation regions are between $\sim$200 pc (which is a limit imposed by the field of view of the VLBA) and $\sim$1 kpc. Higher resolution observations, say with the eMERLIN array at 1.4 GHz is required to probe these regions of jet decollimation. In terms of the relevant scales, a few hundred parsecs is the radius where there is indeed a sharp transition in the physical characteristics of the host galaxy ISM (e.g., R. Launhardt et al. 2002). Changes in pressure equilibrium between the jet and the ambient medium have indeed been suggested to produce jet "flaring" and deceleration on scales of a few kiloparsecs in FRI radio galaxy jets by R. A. Laing & A. H. Bridle (2002). A similar scenario may hold in the relatively lower speed jets in Seyfert and LINER galaxies on shorter distances from their nuclei.

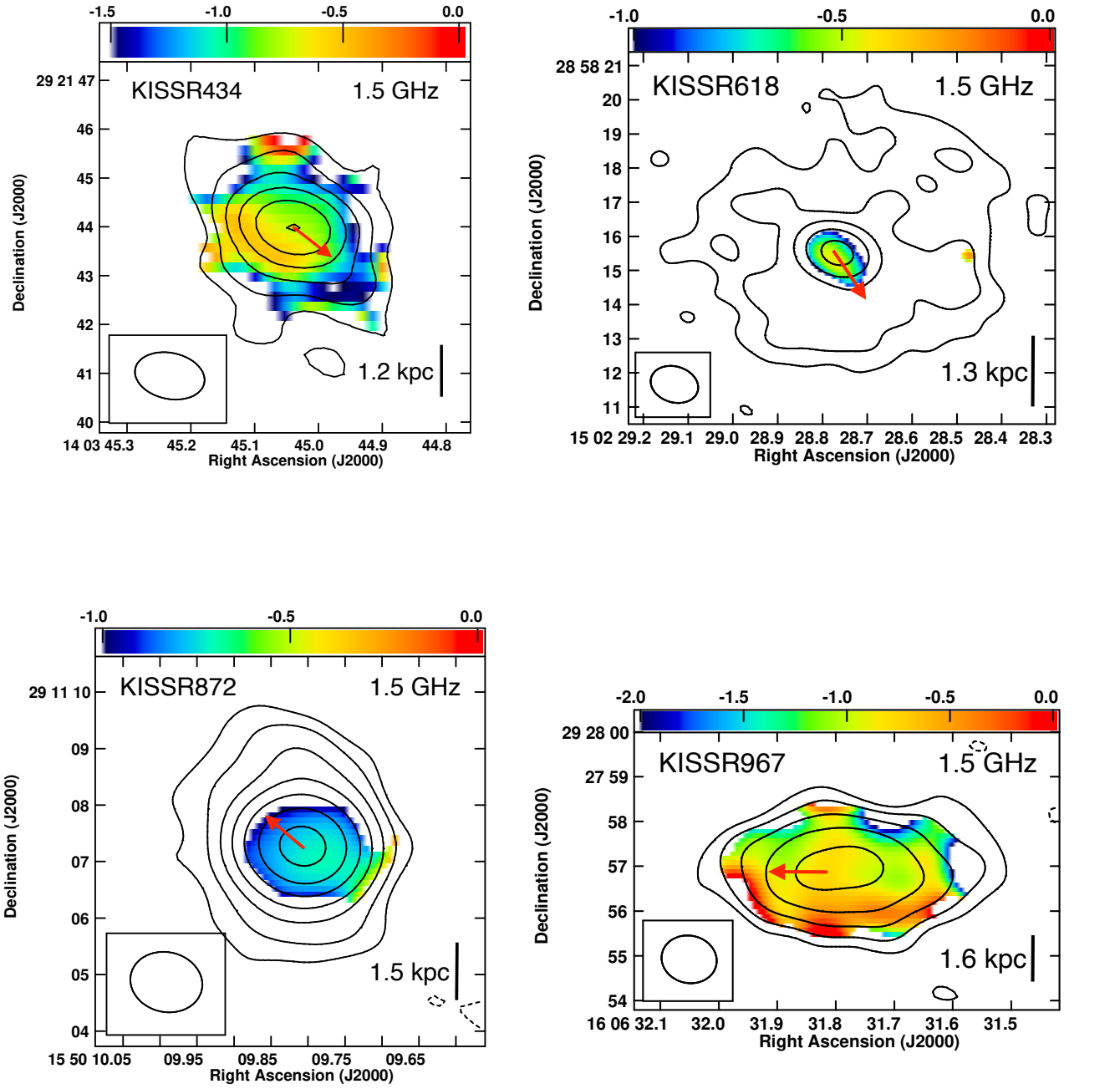

Figure 10. VLA in-band (centered at 1.5 GHz) spectral index images in color of (top left) KISSR434, (top right) KISSR618, (bottom left) KISSR872, and (bottom right) KISSR967. The 1.5 GHz contours are 75 × (1, 2, 4, 8, 16, 32) μJy beam^{-1} for KISSR434, 45 × (± 1, 2, 4, 8, 16) μJy beam^{-1} for KISSR618, 54 × (± 1, 2, 4, 8, 16, 32, 64) μJy beam^{-1} for KISSR872, and 45 × (± 1, 1, 2, 4, 8, 16, 20) μJy beam^{-1} for KISSR967. The red arrow denotes the position angle of the VLBI jet.

6. Discussion

Second epoch VLBI images of eight KISSR galaxies with double-peaked or asymmetric lines in their optical spectra reveal core-jet structures with superluminal jet motions in at least two of them, viz., KISSR102 and KISSR872 (P. Kharb et al. 2024). One of these eight sources, viz. KISSR967, which was detected in epoch-I is not detected in epoch-II. Distinct and compact jet knots that can be identified and traced in both epochs are typically not observed in these radio-faint jets, making the task of speed estimation harder.

A change in jet propagation direction is possibly observed in KISSR618. The jet curvature identified in KISSR434 in epoch-I remains that way 4 yr later in epoch-II. A core-jet structure is identified in KISSR1494 in epoch-II, which was not detected in epoch-I. Overall, the presence of a jet is evident in the VLBI images of all the seven detected KISSR galaxies. Moreover, fast variability in both flux density and parsec-scale radio morphology is evident between two epochs of VLBI data. The average candidate core flux density change for the two sources where the change is significant, viz. KISSR102 and KISSR872, is ≈30%. Similar levels of flux density variability (∼20%–30%) have been observed in other radio-quiet AGN like NGC 5548 (J. M. Wrobel 2000) and NGC 4051 (S. Jones et al. 2011).

In at least four sources, viz. KISSR434, KISSR618, KISSR872, and KISSR1494, but perhaps also in KISR1219, the 1.5 GHz "cores" show diffuse emission extended in a

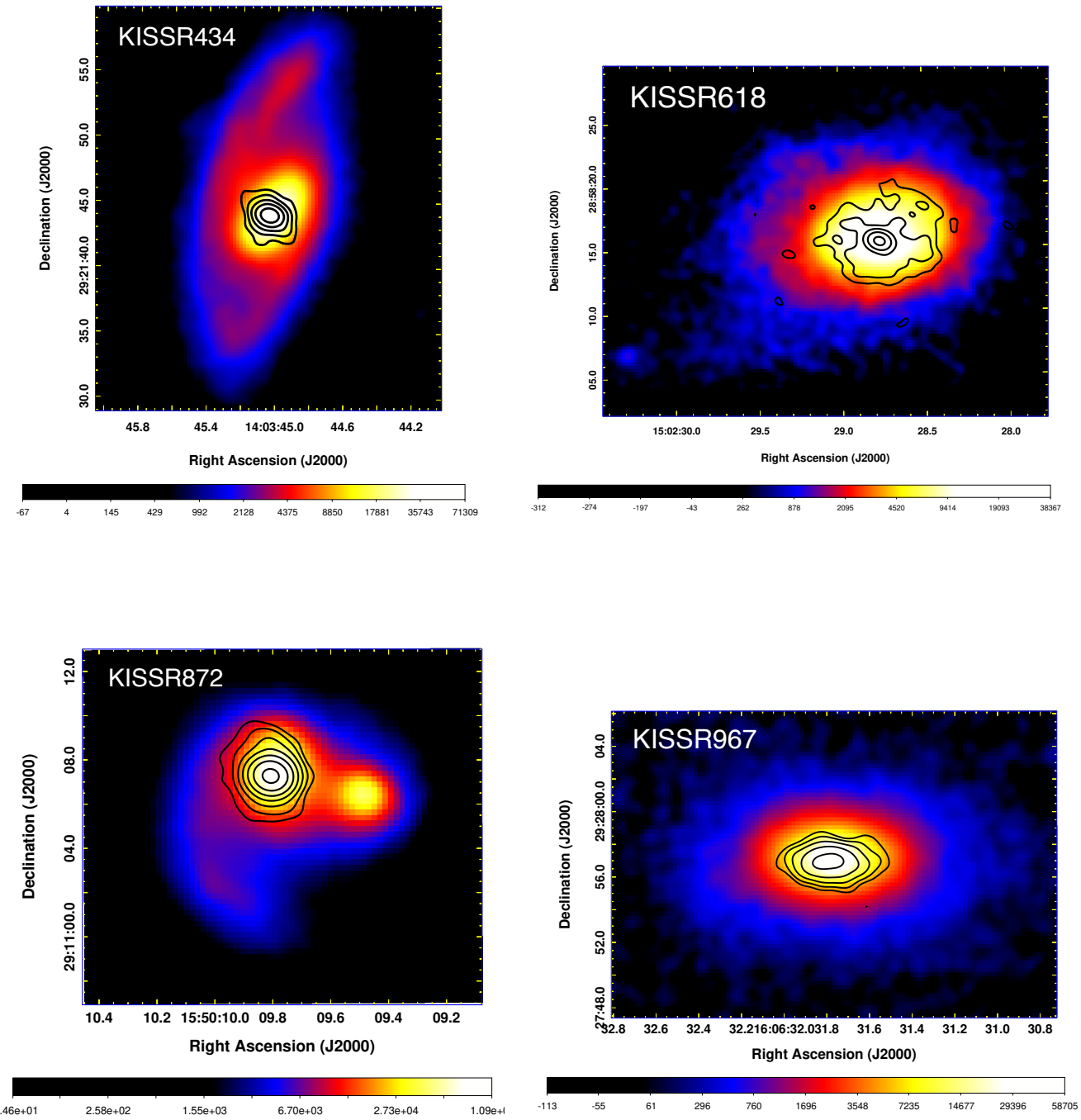

Figure 11. VLA radio contours at 1.5 GHz in black superimposed on color images from Pan-STARRS *i*-band for KISSR434 (top left), KISSR618 (top right), KISSR872 (bottom left), and KISSR967 (bottom right). The contour levels are the same as noted in Figure 10. The FWHM of the synthesized beam is $1\overset{''}{.}44 \times 0\overset{''}{.}94$ at PA $= 78\overset{\circ}{.}2$ for KISSR434, $1\overset{''}{.}42 \times 1\overset{''}{.}05$ at PA $= 73\overset{\circ}{.}4$ for KISSR618, $1\overset{''}{.}28 \times 1\overset{''}{.}06$ at PA $= 77^{\circ}$ for KISSR872, and $1\overset{''}{.}24 \times 1\overset{''}{.}06$ at PA $= 77\overset{\circ}{.}9$ for KISSR967.

transverse direction resembling a broad jet base. Pending their confirmation in future VLBA observations, we discuss some tentative suggestions for their origin. The broad base observed in the RadioAstron image of 3C84 (G. Giovannini et al. 2018) was suggested to arise from the accretion disk. The results from the KISSR sources may be hinting at the existence of jet stratification with either a spine + sheath structure or a jet + (radio-emitting) wind structure on parsec-scales (e.g., R. Nevin et al. 2016; P. Kharb & S. Silpa 2023; S. Silpa et al. 2023; S. Ghosh et al. 2025). A jet+wind structure is also consistent with the flattening of the average core-jet spectral index in KISSR872 (P. Kharb et al. 2024) over a period of 3.7 yr (see Figure 9). The spectral index of KISSR102 became more inverted in epoch-II. This may be consistent with the ejection of a steep-spectrum parsec-scale jet component leaving behind a more compact inverted-spectrum core.

Changes in the direction of jet propagation have been observed in several blazars in the MOJAVE sample (M. L. Lister et al. 2018); these could imply precession of the jet nozzle. A nearly 30° change is observed in the case of KISSR618. Although, the persistence of jet curvature in KISSR434 disfavors jet nozzle precession in that source but rather supports the idea that the jet

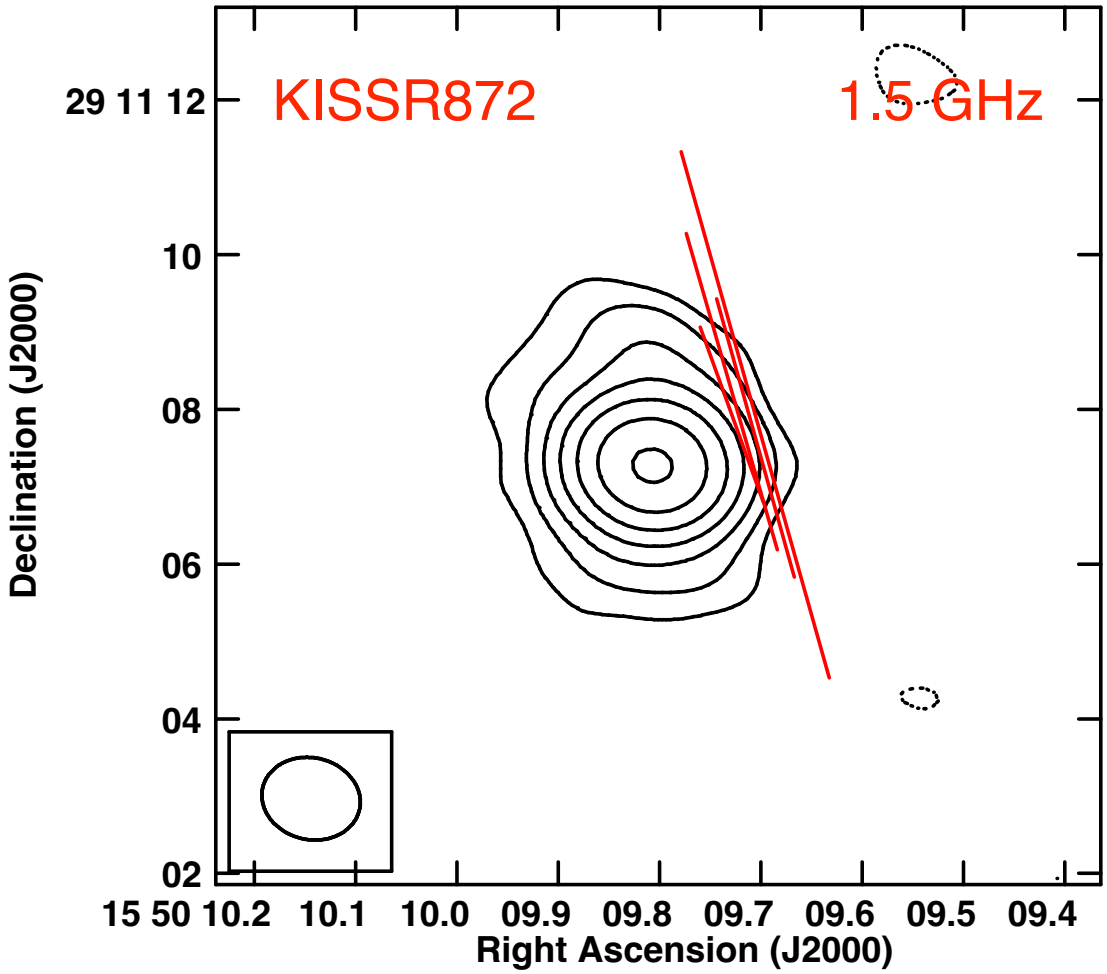

Figure 12. VLA 1.5 GHz image of KISSR872. The radio contours in black are overlaid with polarization vectors in red whose length is proportional to fractional polarization. The contours are 45.36 × (± 1.4, 2.8, 5.6, 11.3, 22.5, 45, 90) μJy beam^{-1}. 1″ of the polarization vector corresponds to a fractional polarization of 6.25%. The FWHM of the synthesized beam is 1.″28 × 1.″06 at PA = 77.°1.

Table 3
Global VLBI Properties

Source Name	Offset (mas)	Gaia Noise (mas)	Flux Density Change (%)	Time Diff. (yr)	Qualitative Findings and a Comparison with Previous Epoch Observations
(1)	(2)	(3)	(4)	(5)	(6)
KISSR102	1.52	8.08	29 ± 7	3.69	Superluminal jet motion with $v = 1.05 \pm 0.45c$
KISSR434	169.24	20.28	14 ± 14	4.85	Broad jet
KISSR618	22.25	12.35	12 ± 14	3.66	Broad jet with jet flaring; jet direction change
KISSR872	38.38[a]	7.14	39 ± 6	3.66	Broad jet; changes b/w epochs; superluminal jet motion with $v = 1.65 \pm 0.57c$
KISSR967	⋯	23.31	>27[b]	3.67	No detection in Epoch-II; weak core with eastern extension detected in Epoch-I
KISSR1154	61.89	32.86	19 ± 20	3.72	No jet detection in Epoch-II; northeastern jet component suggested in Epoch-I
KISSR1219	21.23	5.78	3 ± 20	7.75	Possible broad jet needing confirmation
KISSR1494	40.00	5.07	2 ± 30	9.18	Broad jet, no jet detection in Epoch-I

Notes. Column (1): source name. Column (2): offset between VLBI "core" and Gaia DR3 host galaxy position in milliarcseconds. Column (3): the Gaia *astrometric_excess_noise* parameter in milliarcseconds (see Section 5.1). Column (4): fractional percentage change in the VLBA "core" flux density between two epochs with errors (Section 5.3). Column (5): time difference between the two VLBA epochs in years.
[a] Epoch-I image with a more clearly defined "core" was considered.
[b] KISSR967 was not detected in epoch-II.

plasma flow is along a curved path. Such a behavior has indeed been observed in the blazar 1156+295 (W. Zhao et al. 2011) and the quasar 0836+710 (C. A. Hummel et al. 1992).

While some of the jet behavior in the KISSR sources is reminiscent of that observed in "radio-loud" AGN, there are subtle differences as well. The cores and jet knots in these "radio-quiet" KISSR sources lack the compactness and brightness typically observed in the parsec-scale features of "radio-loud" AGN. This might be indicative of intrinsic differences in the jet composition and/or magnetic field strengths between "radio-loud" and "radio-quiet" AGN (e.g., S. Gulati et al. 2025).

Table 4
Global Properties

Source Name	Black Hole Mass	L_{bol}	S_{FIRST}^{total}	L_6	Eddington Ratio	Q_{jet}	SFR
	($M_\odot$)	(erg s^{-1})	(mJy)	(W Hz^{-1})		(erg s^{-1})	($M_\odot$ yr^{-1})
(1)	(2)	(3)	(4)	(5)	(6)	(7)	(8)
KISSR102	1.7×10^9	6.40×10^{43}	11.3 ± 0.3	4.01×10^{22}	3.0×10^{-4}	8.9×10^{41}	0.30 ± 0.01
KISSR434	1.3×10^8	1.91×10^{44}	6.0 ± 0.3	1.98×10^{22}	0.012	4.9×10^{41}	0.7 ± 0.1
KISSR618	4.6×10^7	1.09×10^{44}	2.5 ± 0.3	1.08×10^{22}	0.018	2.9×10^{41}	0.36 ± 0.03
KISSR872	4.4×10^7	2.26×10^{44}	5.2 ± 0.3	2.96×10^{22}	0.040	6.7×10^{41}	0.93 ± 0.08
KISSR967	1.4×10^8	2.30×10^{43}	2.4 ± 0.2	1.70×10^{22}	0.0013	4.1×10^{41}	1.36 ± 0.20
KISSR1154	3.6×10^7	8.70×10^{43}	3.5 ± 0.8	1.48×10^{22}	0.019	3.8×10^{41}	0.13 ± 0.04
KISSR1219	2.1×10^7	6.19×10^{43}	5.6 ± 0.3	6.11×10^{21}	0.020	1.9×10^{41}	0.40 ± 0.07
KISSR1494	1.4×10^8	4.20×10^{44}	23.0 ± 0.3	6.04×10^{22}	0.020	1.3×10^{42}	1.70 ± 0.09

Note. Column (1): source name. Columns (2) and (3): black hole estimates using the M$-\sigma_\star$ relation and bolometric luminosity, respectively (see Section 5.2 for details). Column (4): total flux density in the VLA FIRST image with errors obtained from the Gaussian-fitting AIPS task JMFIT. Column (5): 6 GHz luminosity extrapolated from VLA FIRST 1.4 GHz data using $\alpha = -0.7$; these are consistent with the sources being "radio-quiet" as defined by K. I. Kellermann et al. (2016). Columns (6) and (7): Eddington ratios and time-averaged jet kinetic power; the latter was derived using the VLA FIRST total flux densities and $\alpha = -0.7$ to convert to 151 MHz flux densities and the relations in B. Punsly & S. Zhang (2011). Column (8): star formation rate derived from the narrow Hα line luminosity (Section 5.2).

Table 5
Results from the VLA 1.5 GHz A-array Observations

Source Name	Total Flux Density	Peak Flux Density	Extd. Flux Density	Average in-band α	Luminosity	SFR1	SFR2
	(mJy)	(mJy)	(mJy)		(W Hz^{-1})	($M_\odot$ yr^{-1})	($M_\odot$ yr^{-1})
(1)	(2)	(3)	(4)	(5)	(6)	(7)	(8)
KISSR434	4.168	2.477	1.691	-0.90 ± 0.06	1.55E+22	4.43	24.37
KISSR618	3.897	0.946	2.952	-0.8 ± 0.1	3.55E+22	8.90	48.96
KISSR872	5.716	4.558	1.159	-0.7 ± 0.3	1.83E+22	4.76	26.18
KISSR967	3.492	0.916	2.576	-0.80 ± 0.06	5.07E+22	13.82	75.99

Note. Column (1): source name. Columns (2), (3), and (4): the total, peak, and extended (total−core) flux density at 1.5 GHz in the VLA images, respectively. Column (5): the average in-band spectral index value. Column (6): the 1.5 GHz total radio luminosity. Columns (7) and (8): the derived star formation rates with stellar masses $\geqslant 5 M_\odot$ and $\geqslant 0.1 M_\odot$, respectively (see Section 5.5.)

The VLBI images of the KISSR galaxies are consistent with the 2D slab-jet simulations of C. J. Saxton et al. (2005), which were used to explain the VLBI images of the compact steep-spectrum (CSS) quasar 3C48. The simulation results of C. J. Saxton et al. (2005) with low density jets propagating in an inhomogeneous medium with a small filling factor of warm, dense clouds, could match what we observe in the VLBI images of the KISSR sources. These outflows are supposed to create bubbles later, which are observed in several Seyfert and LINER galaxies (e.g., P. Kharb et al. 2006; B. Sebastian et al. 2019; S. Ghosh et al. 2025), although not seen in our sources on the spatial scales explored. Apart from the caveats discussed by C. J. Saxton et al. (2005), which include the two-dimensionality of the simulations and the nonrelativistic flows considered, another caveat is that the jet powers considered in C. J. Saxton et al. (2005) fall in the range of 10^{45}–10^{46} erg s^{-1}, whereas the jet powers estimated for the KISSR sources fall in the range of 10^{41}–10^{42} erg s^{-1}.

The jets in the KISSR galaxies are likely to be "light" (see the discussion on a jet-to-ambient-medium density ratio, η, of 10^{-2} in the KISSR434 jet from ram pressure bending and jet kinetic power arguments in P. Kharb et al. 2019) and "fast" (see the relativistic jet motion in KISSR872 in P. Kharb et al. 2024). Fast but light jets are likely to have low kinetic jet powers, consistent with what is obtained for the KISSR sources. As these jets traverse an inhomogeneous medium with a small filling factor, whose characteristics have not been probed so far, they may break or become filamentary on scales of a few 100 pc.

No jetted structures are observed in the VLA images of the four observed galaxies. However, S-shaped lobe-like structures may be present in KISSR434 and KISSR872, which need higher resolution observations to confirm. The kiloparsec-scale spectral index gradients observed in all four sources lies along the VLBI jet directions. This strongly supports the suggestion that the VLA-scale radio emission is predominantly AGN-jet-related. This is consistent with the finding that the SFR derived from the radio luminosity is a factor or a few (for $M \geqslant 5\,M_\odot$) to several orders of magnitude (for $M \geqslant 0.1\,M_\odot$) larger than that derived from the Hα emission lines. Considering both the VLBI and VLA A-array images, the jets likely lose collimation between $\sim$200 pc and $\sim$1 kpc (the lobe-like structures in KISSR434 and KISSR872 extend up to 4 and 5 kpc, respectively).

Kiloparsec-scale polarization is only detected in the LINER galaxy KISSR872. Interestingly, the region of high fractional polarization is in the same direction as the second optical nucleus present in this interacting galaxy. The inferred magnetic field in this optically thin region is perpendicular to the polarization vectors (A. G. Pacholczyk 1970), as well as this northern fainter tidal tail. This is suggestive of compressed gas and magnetic fields as the gas gets tidally pulled from the secondary nucleus by the primary nucleus. KISSR872 resembles the interacting galaxy NGC 6240, which is in a late-stage merger and possesses a bridge of hot, turbulent gas

in between its two optical nuclei (E. Treister et al. 2020; L. Hermosa Muñoz et al. 2025).

7. Summary and Conclusions

We have presented the second-epoch phase-referenced VLBA images of eight KISSR galaxies at 1.5 GHz and three of them being observed at 5 GHz as well. We summarize the primary findings below.

1. We detect emission in seven out of eight KISSR galaxies at 1.5 GHz in the second-epoch of VLBI observations; KISSR967 was not detected in this epoch. We detect emission in two out of three sources at 5 GHz in epoch-II observations; KISSR434 was not detected at 5 GHz in this epoch. Changes are observed in the flux density, spectral index, jet features, and jet propagation directions in these galaxies. In one source, viz. KISSR434, the jet curvature remains after a period of 4 yr, while in another source, viz. KISSR618, the jet direction may have changed by nearly 30°. Such a behavior in parsec-scale jets is also observed in the VLBI observations of "radio-loud" AGN.
2. Superluminal jet motion is observed in the jets of two LINER galaxies, viz., KISSR102 and KISSR872 (P. Kharb et al. 2024). The determination of jet speeds in other sources is made difficult by the presence of diffuse jet components, which are hard to identify between epochs. Multiepoch VLBI observations are necessary to study the jets in Seyfert and LINER galaxies.
3. Substructures are observed in the cores and jets of several sources possibly indicating jet stratification on parsec-scales. Relatively broad jets might be consistent with "jet+wind" structures or "spine+sheath" structures. This might be a result of jet–medium interaction as suggested in the jet simulations of C. J. Saxton et al. (2005). Faster lighter jets moving in inhomogeneous media with small filling factors could explain these VLBI results.
4. The VLA images of four KISSR sources reveal core-halo or core-lobe structures. The alignment of the parsec-scale jets with the kiloparsec-scale spectral index gradients from flat-to-steep is consistent with an AGN-jet-related origin of the VLA emission. A large mismatch between the SFR (5–25 for stellar masses $M \geqslant 5M_{\odot}$) derived from the radio emission and Hα line emission also supports an AGN origin for the radio emission. A comparison of the VLBA and VLA images suggests that the jets in the KISSR sources lose collimation on spatial scales between 200 pc and 1 kpc.
5. Signatures of jet-mode AGN feedback on kiloparsec-scales may be present in KISSR102. However, sub-kiloparsec-scale images are needed to confirm the presence of a jet on these scales. The jet–medium interaction has also been invoked to explain the emission-line analysis in P. Kharb et al. (2021) as well as the presence of double peaks and asymmetries in the emission lines in KISSR sources.

Overall, our two-epoch VLBI study of eight KISSR Seyfert and LINER galaxies strongly supports the presence of ∼100 pc-scale jets in these "radio-quiet" AGN. The behavior of these jets is similar to the pc-scale jets observed in "radio-loud" AGN, although they are highly scaled down in terms of total radio power. There are, however, subtle differences as well. The cores and jet knots in these "radio-quiet" sources lack the compactness and brightness typically observed in the parsec-scale features of "radio-loud" AGN. This might be indicative of intrinsic differences in the jet composition and/or magnetic field strengths between "radio-loud" AGN and "radio-quiet" AGN.

Acknowledgments

We thank the anonymous referee for their comments that have improved this manuscript significantly. P.K. and S.G. acknowledge the support of the Department of Atomic Energy, Government of India, under the project 12-R&D-TFR-5.02-0700. P.K. acknowledges the useful suggestions from Silpa Sasikumar on EVLA data analysis. M.D. gratefully acknowledges the support of the Department of Science and Technology (DST) grant DST/WIDUSHIA/PM/PM/2023/25(G) for this research. D.A.S. was supported by NASA contract NAS8-03060 to the Chandra X-ray Center, and by Chandra X-ray Center grant GO2-23097X. The National Radio Astronomy Observatory is a facility of the National Science Foundation operated under cooperative agreement by Associated Universities, Inc. The VLBA data were calibrated using NRAO's "VLBA data calibration pipeline" in AIPS. This work has made use of data from the European Space Agency (ESA) mission Gaia.

Facilities: VLBA, VLA, Gaia.

Software: AIPS (E. W. Greisen 2003), CASA (J. P. McMullin et al. 2007).

ORCID iDs

Preeti Kharb https://orcid.org/0000-0003-3203-1613
Anderson Caproni https://orcid.org/0000-0001-9707-3895
Salmoli Ghosh https://orcid.org/0009-0000-1447-5419
Daniel A. Schwartz https://orcid.org/0000-0001-8252-4753
Mousumi Das https://orcid.org/0000-0001-8996-6474
Smitha Subramanian https://orcid.org/0000-0002-5331-6098
Sravani Vaddi https://orcid.org/0000-0003-3295-6595

References

Antonucci, R. 1993, ARA&A, 31, 473
Antonucci, R. R. J., & Miller, J. S. 1985, ApJ, 297, 621
Baldi, R. D., Williams, D. R. A., McHardy, I. M., et al. 2018, MNRAS, 476, 3478
Baum, S. A., O'Dea, C. P., Dallacassa, D., de Bruyn, A. G., & Pedlar, A. 1993, ApJ, 419, 553
Becker, R. H., White, R. L., & Helfand, D. J. 1995, ApJ, 450, 559
Bontempi, P., Giroletti, M., Panessa, F., Orienti, M., & Doi, A. 2012, MNRAS, 426, 588
Caproni, A., Abraham, Z., Motter, J. C., & Monteiro, H. 2017, ApJL, 851, L39
Caproni, A., Melo, I. T., Abraham, Z., Monteiro, H., & Roland, J. 2014, MNRAS, 441, 187
Caproni, A., Monteiro, H., Abraham, Z., Teixeira, D. M., & Toffoli, R. T. 2011, ApJ, 736, 68
Cheng, X., Yang, J., Zhao, G.-Y., et al. 2023, ApJL, 955, L30
Chiaraluce, E., Bruni, G., Panessa, F., et al. 2019, MNRAS, 485, 3185
Cirasuolo, M., Celotti, A., Magliocchetti, M., & Danese, L. 2003, MNRAS, 346, 447
Colbert, E. J. M., Baum, S. A., Gallimore, J. F., O'Dea, C. P., & Christensen, J. A. 1996, ApJ, 467, 551
Comerford, J. M., Nevin, R., Stemo, A., et al. 2018, ApJ, 867, 66
Condon, J. J. 1992, ARA&A, 30, 575
Condon, J. J., Cotton, W. D., & Broderick, J. J. 2002, AJ, 124, 675

Doi, A., Kohno, K., Nakanishi, K., et al. 2013, ApJ, 765, 63
Falcke, H., Nagar, N. M., Wilson, A. S., & Ulvestad, J. S. 2000, ApJ, 542, 197
Fischer, T. C., Crenshaw, D. M., Kraemer, S. B., et al. 2011, ApJ, 727, 71
Fu, H., Yan, L., Myers, A. D., et al. 2012, ApJ, 745, 67
Gallimore, J. F., Axon, D. J., O'Dea, C. P., Baum, S. A., & Pedlar, A. 2006, AJ, 132, 546
Ge, J.-Q., Hu, C., Wang, J.-M., Bai, J.-M., & Zhang, S. 2012, ApJS, 201, 31
Gerke, B. F., Newman, J. A., Lotz, J., et al. 2007, ApJL, 660, L23
Ghosh, S., Kharb, P., Sebastian, B., et al. 2025, arXiv:2509.15355
Giovannini, G., Savolainen, T., Orienti, M., et al. 2018, NatAs, 2, 472
Giroletti, M., & Panessa, F. 2009, ApJL, 706, L260
Greisen, E. W. 2003, ASSL, 285, 109
Gulati, S., Sasikumar, S., Kharb, P., et al. 2025, ApJS, 281, 56
Heckman, T. M., & Best, P. N. 2014, ARA&A, 52, 589
Heckman, T. M., Kauffmann, G., Brinchmann, J., et al. 2004, ApJ, 613, 109
Hermosa Muñoz, L., Alonso-Herrero, A., Labiano, A., et al. 2025, A&A, 693, A321
Ho, L. C. 2008, ARA&A, 46, 475
Hummel, C. A., Muxlow, T. W. B., Krichbaum, T. P., et al. 1992, A&A, 266, 93
Jones, S., McHardy, I., Moss, D., et al. 2011, MNRAS, 412, 2641
Kellermann, K. I., Condon, J. J., Kimball, A. E., Perley, R. A., & Ivezić, Ž. 2016, ApJ, 831, 168
Kellermann, K. I., Sramek, R., Schmidt, M., Shaffer, D. B., & Green, R. 1989, AJ, 98, 1195
Kennicutt, R. C., Jr. 1998, ApJ, 498, 541
Khachikian, E. Y., & Weedman, D. W. 1974, ApJ, 192, 581
Kharb, P., Blackman, E. G., Clausen-Brown, E., et al. 2024, ApJ, 962, 180
Kharb, P., Das, M., Paragi, Z., Subramanian, S., & Chitta, L. P. 2015, ApJ, 799, 161
Kharb, P., Lal, D. V., & Merritt, D. 2017a, NatAs, 1, 727
Kharb, P., Lena, D., Paragi, Z., et al. 2020, ApJ, 890, 40
Kharb, P., O'Dea, C. P., Baum, S. A., Colbert, E. J. M., & Xu, C. 2006, ApJ, 652, 177
Kharb, P., & Silpa, S. 2023, Galax, 11, 27
Kharb, P., Subramanian, S., Das, M., Vaddi, S., & Paragi, Z. 2021, ApJ, 919, 108
Kharb, P., Subramanian, S., Vaddi, S., Das, M., & Paragi, Z. 2017b, ApJ, 846, 12
Kharb, P., Vaddi, S., Sebastian, B., et al. 2019, ApJ, 871, 249
Klindt, L., Alexander, D. M., Rosario, D. J., Lusso, E., & Fotopoulou, S. 2019, MNRAS, 488, 3109
Laing, R. A., & Bridle, A. H. 2002, MNRAS, 336, 1161
Launhardt, R., Zylka, R., & Mezger, P. G. 2002, A&A, 384, 112
Lind, K. R., & Blandford, R. D. 1985, ApJ, 295, 358
Lindegren, L., Hernández, J., Bombrun, A., et al. 2018, A&A, 616, A2
Lindegren, L., Klioner, S. A., Hernández, J., Bombrun, A., et al. 2021, A&A, 649, A2
Lister, M. L., Aller, M. F., Aller, H. D., et al. 2018, ApJS, 234, 12
Liu, X., Shen, Y., Strauss, M. A., & Greene, J. E. 2010, ApJ, 708, 427
Maschmann, D., Halle, A., Melchior, A.-L., Combes, F., & Chilingarian, I. V. 2023, A&A, 670, A46
McConnell, N. J., & Ma, C.-P. 2013, ApJ, 764, 184
McMullin, J. P., Waters, B., Schiebel, D., Young, W., & Golap, K. 2007, ASPC, 376, 127
Miniutti, G., Sanfrutos, M., Beuchert, T., et al. 2014, MNRAS, 437, 1776
Müller-Sánchez, F., Comerford, J. M., Nevin, R., et al. 2015, ApJ, 813, 103
Mundell, C. G., Wilson, A. S., Ulvestad, J. S., & Roy, A. L. 2000, ApJ, 529, 816
Nandi, S., Kharb, P., Caproni, A., Roy, R., & Sebastian, B. 2024, ApJ, 965, 9
Nevin, R., Comerford, J., Müller-Sánchez, F., Barrows, R., & Cooper, M. 2016, ApJ, 832, 67
Orienti, M., & Prieto, M. A. 2010, MNRAS, 401, 2599
Osterbrock, D. E. 1978, PNAS, 75, 540
Pacholczyk, A. G. 1970, Radio Astrophysics. Nonthermal Processes in Galactic and Extragalactic Sources (Freeman)
Peterson, B. M. 1997, An Introduction to Active Galactic Nuclei (Cambridge Univ. Press)
Punsly, B., & Zhang, S. 2011, ApJL, 735, L3
Rao, V. V., Kharb, P., Rubinur, K., et al. 2023, MNRAS, 524, 1615
Rees, M. J. 1984, ARA&A, 22, 471
Rosario, D. J., Shields, G. A., Taylor, G. B., Salviander, S., & Smith, K. L. 2010, ApJ, 716, 131
Roy, A. L., Ulvestad, J. S., Wilson, A. S., et al. 2000, in Perspectives on Radio Astronomy: Science with Large Antenna Arrays, ed. M. P. van Haarlem (ASTRON), 173
Rubinstein, R. Y. 1997, EJOR, 99, 89
Saxton, C. J., Bicknell, G. V., Sutherland, R. S., & Midgley, S. 2005, MNRAS, 359, 781
Schmitt, H. R., Antonucci, R. R. J., Ulvestad, J. S., et al. 2001, ApJ, 555, 663
Sebastian, B., Kharb, P., O'Dea, C. P., Colbert, E. J. M., & Baum, S. A. 2019, ApJ, 883, 189
Shen, Y., Liu, X., Greene, J. E., & Strauss, M. A. 2011, ApJ, 735, 48
Silpa, S., Kharb, P., Ho, L. C., & Harrison, C. M. 2023, ApJ, 958, 47
Simpson, C., Mulchaey, J. S., Wilson, A. S., Ward, M. J., & Alonso-Herrero, A. 1996, ApJL, 457, L19
Smith, K. L., Shields, G. A., Salviander, S., Stevens, A. C., & Rosario, D. J. 2012, ApJ, 752, 63
Spinoglio, L., Fernández-Ontiveros, J. A., & Malkan, M. A. 2024, ApJ, 964, 117
Sumida, V. Y. D., Schutzer, A. d. A., Caproni, A., & Abraham, Z. 2021, MNRAS, 509, 1646
Terashima, Y., & Wilson, A. S. 2003, ApJ, 583, 145
Treister, E., Messias, H., Privon, G. C., et al. 2020, ApJ, 890, 149
Ulvestad, J. S., & Ho, L. C. 2001, ApJL, 562, L133
Wang, A., An, T., Kellermann, K. I., et al. 2025, ApJL, 987, L26
Wang, J.-M., Chen, Y.-M., Hu, C., et al. 2009, ApJL, 705, L76
Wegner, G., Salzer, J. J., Jangren, A., Gronwall, C., & Melbourne, J. 2003, AJ, 125, 2373
White, R. L., Becker, R. H., Gregg, M. D., et al. 2000, ApJS, 126, 133
Whittle, M., Pedlar, A., Meurs, E. J. A., et al. 1988, ApJ, 326, 125
Wilson, A. S., & Colbert, E. J. M. 1995, ApJ, 438, 62
Woltjer, L. 1990, in Active Galactic Nuclei, ed. R. D. Blandford et al. (Springer), 1
Wrobel, J. M. 2000, ApJ, 531, 716
York, D. G. & SDSS Collaboration 2000, AJ, 120, 1579
Younes, G., Porquet, D., Sabra, B., Reeves, J. N., & Grosso, N. 2012, A&A, 539, A104
Zhang, Z., Chen, Y., Shen, S., et al. 2025, MNRAS, 543, 3089
Zhao, W., Hong, X. Y., An, T., et al. 2011, A&A, 529, A113
Zhou, H., Wang, T., Zhang, X., Dong, X., & Li, C. 2004, ApJL, 604, L33